



Microstructures Reveal Mechanical Compaction and Volatile-Rich Liquid Migration in the Layered Alkaline Ilímaussaq Complex, South Greenland

EMILY JONES ¹, WILLIAM MCCARTHY¹, SANDRA PIAZOLO², CRAIG MAGEE ², MADELEINE C.S. HUMPHREYS³ and WILL HUTCHISON¹

¹ School of Earth and Environmental Sciences, University of St Andrews, Bute Building, Queen's Terrace, St Andrews KY16 9TS, UK

² School of Earth and Environment, University of Leeds, Woodhouse, Leeds LS2 9NH, UK

³ Department of Earth Sciences, Durham University, Arthur Holmes Building, Science Site, South Road, Durham DH1 3LE, UK

*Corresponding author. Telephone: +44 7508418222. E-mail: em208@st-andrews.ac.uk

[†] Handling Editor: Prof. Valentin Troll

Crystal–melt separation is a fundamental process in magmatic differentiation that has implications for volcanic eruptions and ore deposit formation. However, the mechanical processes governing how crystals and melt separate, which are important for the timescales of melt segregation, are debated. Geochemical and theoretical studies commonly cite viscous compaction, i.e. gravitationally or intrinsic stress-driven deformation of the crystal pile, as a key mechanism of crystal–melt separation. Critically, viscous compaction should produce a microstructural record of internal crystal deformation and crystal alignment that allows us to diagnose its role, if any, in crystal–melt separation. Here, we provide novel textural and microstructural data from the Ilímaussaq complex, a layered alkaline intrusion in South Greenland, and explore whether, and if so through what processes, crystal–melt separation within the crystal pile. Stratigraphically variable disequilibrium and nucleation microstructures within our samples record the vertical migration of interstitial volatile-rich liquid through igneous layers. We observe some mineral bending associated with asymmetrical crystal growth, but no evidence of extensive viscous grain deformation, indicating that viscous compaction was not a significant mechanism in crystal–melt separation for Ilímaussaq. Instead, we suggest that mechanical compaction via crystal rearrangement, accompanied by volatile-rich liquid migration, primarily facilitates crystal–melt separation in intrusions with chemically evolved compositions. Our study shows that post-cumulus crystal repacking and volatile-rich liquid movement impact primary igneous layering in terms of microstructures, modal abundances of main and minor phases as well as phase compositions, therefore potentially controlling the distribution and concentration of rare earth element deposits within layered alkaline intrusions.

Key words: compaction; layered intrusion; microstructure; Ilímaussaq

INTRODUCTION

The separation of crystals from melt is crucial to accumulating large volumes of eruptible magma and concentrating ore-bearing minerals within layered igneous intrusions (e.g. Boudreau & McCallum, 1992; Mathez *et al.*, 1997; Boudreau & Meurer, 1999; Meurer *et al.*, 1999; Bachmann & Bergantz, 2004; Vukmanovic *et al.*, 2019). Although phase separation is understood to be a widespread phenomenon in igneous rocks, the mechanical process of how crystals and melt separate within a magma is debated (e.g. Gray *et al.*, 2003; Philpotts & Philpotts, 2005; Holness *et al.*, 2017; Holness, 2018; Bachmann & Huber, 2019; Latypov *et al.*, 2024). Mechanisms invoked to explain crystal–melt separation include: (1) mechanical compaction through crystal rearrangement in mushes with crystallinities up to the maximum packing threshold (~30–90% depending on crystal shape and size) (e.g. Philpotts & Philpotts, 2005; Bachmann & Huber, 2019; Florez *et al.*, 2024); (2) viscous compaction of the crystal pile involving gravitationally or intrinsic stress-driven viscous grain deformation and expulsion of liquid when crystallinities approach the maximum

packing fraction (e.g. Irvine, 1980; Thy *et al.*, 2009; Mckenzie, 2011; Schmidt *et al.*, 2012; Lissenberg *et al.*, 2019; Connolly & Schmidt, 2022); (3) magma recharge and/or flow, which could cause thermal rejuvenation or shear-enhanced mechanical compaction due to lateral magmatic flow (e.g. Irvine *et al.*, 1998; Lissenberg *et al.*, 2019; Vukmanovic *et al.*, 2019; Gleeson *et al.*, 2023); (4) compositional or thermal convection of interstitial liquid (e.g. Sparks *et al.*, 1985; Kerr & Tait, 1986; Tait & Jaupart, 1992); or (5) gas filter-pressing, during which volatile exsolution creates pressure gradients causing the migration of liquid through the crystal pile (Anderson *et al.*, 1984; Sisson & Bacon, 1999; Boudreau, 2016). These mechanisms of crystal–melt separation may leave behind a microstructural record, such that microstructural studies of cumulate rocks can be used to test their contribution to phase separation (e.g. Philpotts & Philpotts, 2005; Holness *et al.*, 2017; Holness, 2018; Bertolett *et al.*, 2019; Vukmanovic *et al.*, 2019).

Theoretical and geochemical studies typically favour viscous compaction as a primary mechanism for interstitial liquid extraction from mushes with intermediate to high crystallinities (Mckenzie, 1984, 2011; Sparks *et al.*, 1985; Tharp *et al.*, 1998;

RECEIVED MARCH 19, 2025; REVISED JULY 18, 2025; ACCEPTED JULY 22, 2025

© The Author(s) 2025. Published by Oxford University Press.

This is an Open Access article distributed under the terms of the Creative Commons Attribution License (<https://creativecommons.org/licenses/by/4.0/>), which permits unrestricted reuse, distribution, and reproduction in any medium, provided the original work is properly cited.

Tegner *et al.*, 2009; Schmidt *et al.*, 2012; Latypov *et al.*, 2024). During viscous compaction, gravitational loading results in high localised stresses at crystal–crystal interfaces and triggers viscous deformation, which changes the shape of crystals and distorts their internal structure (Hirth & Kohlstedt, 1995; Tharp *et al.*, 1998; Meurer & Boudreau, 1998b; Connolly & Schmidt, 2022). This viscous deformation may occur by several different deformation mechanisms, including dislocation generation and movement (i.e. dislocation creep and/or deformation twinning), dissolution at high-stress interfaces and precipitation in low-stress domains (i.e. dissolution–precipitation creep, pressure solution creep), or diffusion creep where crystal lattice vacancies diffuse along boundaries or through the crystals (e.g. Hirth & Kohlstedt, 1995; Mei *et al.*, 2002; Scott & Kohlstedt, 2006; Svahnberg & Piazzolo, 2010, 2013). As the term viscous compaction does not distinguish specific processes in crystal–melt separation, herein we refer directly to compaction via viscous grain deformation, or more specifically, compaction via dislocation creep, dissolution–precipitation creep, or via diffusion creep.

Few studies have used diagnostic microstructural criteria to decipher the nature of crystal–melt separation mechanisms in layered igneous rocks. Those that do focus on mafic–ultramafic systems, leaving a clear gap in our knowledge of crystal–melt separation processes active within layered alkaline intrusions (Gray *et al.*, 2003; Philpotts & Philpotts, 2005; Holness *et al.*, 2017; Bertolett *et al.*, 2019; Vukmanovic *et al.*, 2019). Alkaline intrusions represent some of the most chemically evolved and volatile-rich igneous systems and therefore may have different crystal–melt separation mechanisms than their mafic–ultramafic counterparts (e.g. Hunter, 1987; Sorensen, 1997; Holness *et al.*, 2017; Marks & Markl, 2017). As alkaline layered intrusions host some of the world’s largest deposits of rare earth elements (REEs) and high field strength elements, uncovering the mechanisms of crystal–melt separation is crucial for understanding how critical minerals are concentrated within these intrusions (e.g. Schønswandt *et al.*, 2016; Smith & Maier, 2021; Beard *et al.*, 2023).

Here, we present a detailed microstructural study of layered nepheline syenites from Ílmaussaq, an alkaline-layered intrusion in South Greenland that hosts a world-class REE deposit (Ferguson, 1964; Bohse *et al.*, 1971; Upton, 2013; Schønswandt *et al.*, 2016). We present characteristics of the microstructures observed and consider their broader geological context to interpret the mechanisms of crystal–melt separation. Despite the presence of apparently bent crystals, our samples show clear evidence of vertical migration of the interstitial liquid, with little to no evidence of viscous grain deformation. Our findings support the growing body of microstructural evidence that compaction via viscous grain deformation is likely not an important mechanism for crystal–melt separation, particularly in intrusions with more evolved compositions such as Ílmaussaq. Variable dominance of disequilibrium, deformation, and nucleation microstructures across compositionally distinct, primary igneous layers suggest that crystal repacking (i.e. mechanical compaction) in combination with volatile-rich liquid migration through these layers is most likely to dominate crystal–melt separation processes in alkaline intrusions.

IGNEOUS MICROSTRUCTURES

Microstructures within igneous rocks record the final product of processes that occurred throughout their crystallisation history (e.g. Higgins, 2015; Holness *et al.*, 2017). To unravel microstructural evidence of crystal–melt separation, the timing and interaction

of all microstructures must be considered, as the presence or lack of any one microstructure seldom provides definitive proof of an overarching process (e.g. Higgins, 2015; Holness & Vernon, 2015; Holness *et al.*, 2017, 2018). Here, we discuss the various microstructures recorded in magmatic rocks, and the petrological processes they are understood to reflect.

Early crystallisation microstructures

Crystal shapes, boundaries, and junctions help distinguish between early crystal growth and more evolved textures (Holness & Siklos, 2000; Holness *et al.*, 2005, 2007, 2019). Primary textures record crystal growth in liquid-rich environments and reflect interfacial growth kinetics, which typically produce euhedral crystals with straight grain boundaries (Fig. 1a) (e.g. Holness *et al.*, 2005, 2017, 2019; Higgins, 2015). However, if multiple crystals grow simultaneously, impingement of adjacent crystals may cause their boundaries to interfere and/or wrap around one another (Fig. 1a) (Holness *et al.*, 2005; Higgins, 2011). During primary crystal growth, the geometry of liquid-filled pores is controlled by the orientation, size distribution, and shape of grains (e.g. Higgins, 2015). Liquid-filled pores are thus typically irregular in shape and form in small spaces between larger primocrysts (Fig. 1a) (Holness *et al.*, 2019). Liquid may be preserved as thin glassy films along grain boundaries and at three-grain junctions, or replaced by interstitial minerals during late-stage crystallisation (e.g. Holness *et al.*, 2011, 2019). By identifying these liquid-filled pores, whether filled with glass or minerals, we can distinguish between interstitial and primocryst minerals (Wager *et al.*, 1960). The proportion of interstitial to primocryst minerals may therefore be used as a rough, minimum estimate (as interstitial minerals do not include any interstitial overgrowth on primocryst minerals) of the amount of residual liquid within a mush (Wager *et al.*, 1960).

Microstructures such as oikocrysts, glomerocrysts, and crystal clusters also indicate the presence of a liquid-rich environment (Fig. 1b and c). Oikocrysts are thought to form as an interstitial phase from interstitial liquid within a mush, although this has been challenged by suggestions that they form *in situ* as primocryst phases (Wager *et al.*, 1960; Barnes *et al.*, 2016; Latypov *et al.*, 2020). Oikocrysts interpreted as *in situ* primocryst phases should lack significant zoning and be present in cotectic proportions with other primocrysts (e.g. Jackson, 1961; Latypov *et al.*, 2020). Glomerocrysts or crystal clusters are indicators of liquid presence as they form through synneusis and/or accumulation (aggregation), or through heterogeneous nucleation in a liquid-rich environment during early crystal settling or during mush disaggregation (e.g. Seaman, 2000; Hammer *et al.*, 2010; Moore *et al.*, 2014; Sliwinski *et al.*, 2015; Zhu *et al.*, 2018; Lissenberg *et al.*, 2019). The formation of clusters through heterogeneous nucleation may occur within a mush as small crystal fragments act as nuclei upon which other crystals nucleate and grow (Hammer *et al.*, 2010; Holness *et al.*, 2023). While clusters that form through heterogeneous nucleation tend to be polymineralic, they may appear to be monomineralic if the nucleation substrate is not visible (Holness *et al.*, 2023). Heterogeneous nucleation typically results in a strong clustering of elongate crystals that radiate away from the site of nucleation, sometimes referred to as stellite clusters (Fig. 1c) (Parsons, 1979; Sorensen, 1992; Špillar & Dolejš, 2015). Clusters that form via aggregation develop either by impingement of grains growing in proximity (evidenced by anhedral grains connected along irregular grain boundaries), or by accumulation in a convecting/flowing liquid (evidenced by

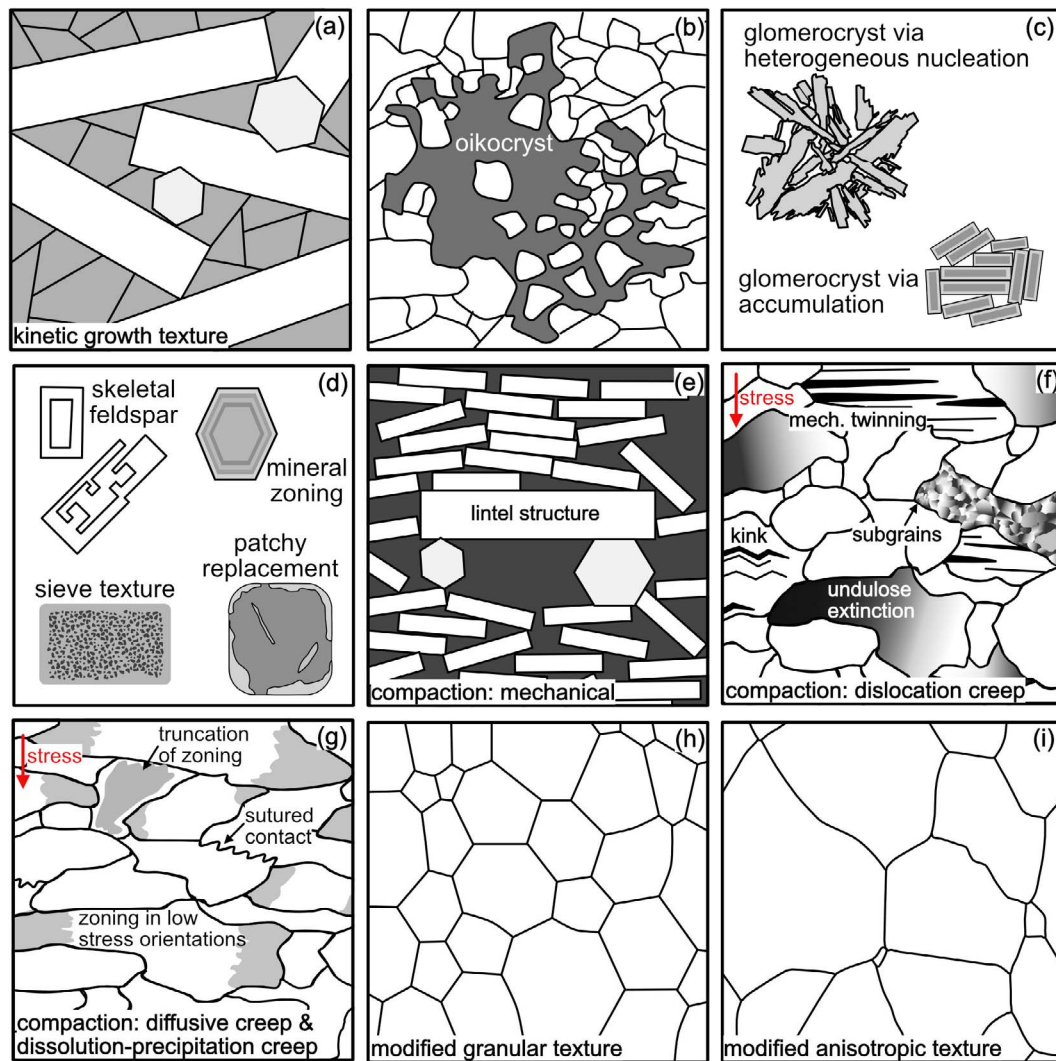


Fig. 1. Schematic examples of some igneous microstructures and textures. (a) Schematic of texture resulting from crystal growth in a melt-rich environment; (b) example of an oikocryst with enclosed chadacrysts; (c) example of plagioclase glomerocryst formed via heterogeneous nucleation modified from McCarthy *et al.* (2020), and example of plagioclase glomerocryst formed via accumulation; (d) common disequilibrium microstructures; (e) schematic of lintel structure formed during mechanical compaction; (f) schematic of microstructures formed during compaction via dislocation creep; (g) schematic of microstructures formed during compaction via diffusion and dissolution-precipitation creep; (h) schematic of modified granular texture in a monomineralic rock modified from Bons *et al.* (2001); and (i) schematic of modified anisotropic texture in a monomineralic rock modified from Piazzolo *et al.* (2016).

ehedral grains connected along planar grain boundaries, Fig. 1c) (Schwindinger, 1999; Holness *et al.*, 2019, 2023; Marsh *et al.*, 2021).

Chemical disequilibrium microstructures

Crystals that are in chemical disequilibrium with surrounding liquid in a mush may dissolve, replace, grow, and/or diffusively equilibrate (e.g. Couch *et al.*, 2001; Streck, 2008; Putnis, 2009; Holness *et al.*, 2011; Humphreys, 2011; Asimus *et al.*, 2024; Mangler *et al.*, 2024). In the context of crystal mush formation in a layered intrusion, crystal-liquid disequilibrium particularly occurs when a liquid infiltrates a compositionally different mush layer, perhaps in response to magma mixing or convection (e.g. Irvine, 1980; Chadam *et al.*, 1986; Spiegelman *et al.*, 2001; Solano *et al.*, 2014; Lissenberg & MacLeod, 2016; Jackson *et al.*, 2018; Sanfilippo *et al.*, 2020; Koopmans *et al.*, 2022). The infiltration of a liquid into a mush layer may result in resorption, where primocrysts are assimilated and a new generation of minerals crystallise that diverge from the expected liquid line of descent

(Boulanger & France, 2023). Changes in intensive parameters such as temperature, pressure, or volatile content may also result in chemical disequilibrium between liquid and crystals (e.g. Streck, 2008; Mangler *et al.*, 2024; Nikolenko *et al.*, 2024). A common chemical disequilibrium microstructure is fluid-mediated, interface-coupled mineral replacement, where an original mineral, no longer in chemical equilibrium with the surrounding liquid, is replaced with a more stable chemical composition in the solid solution series of a particular phase (e.g. feldspar, (Putnis, 2009)). The shape of the reaction front can vary from smooth to highly irregular (Koehn *et al.*, 2021). Such melt-mediated mineral replacement may be patchy, associated with high porosity in the replaced phases, forming a sieve or pothole structure, and/or produce mineral boundaries that are irregular (Fig. 1d) (e.g. Stewart & Pearce, 2004; Streck, 2008; Mangler *et al.*, 2024). In contrast, if minerals become unstable at low temperatures (e.g. ternary feldspars) exsolution microstructures rather than melt-mediated replacement microstructures are seen, where

the newly formed exsolved phases are more evenly distributed rather than patchy (e.g. [Schönwandt et al., 2023](#)). If the original mineral and replacing mineral have similar crystal structures, then mineral replacement may show epitaxy, where the newly forming mineral takes on, at least in part, the crystallographic orientation of the replaced mineral (e.g. [Putnis, 2002, 2009](#)).

Other signatures of chemical disequilibrium include compositional zoning such as oscillatory or concentric zoning, which are typically associated with compositional changes within a liquid (Fig. 1d) ([Streck, 2008; Borst et al., 2018](#)). Feldspar morphologies such as resorption textures and skeletal growth are also indicators of various types of disequilibrium (Fig. 1d) ([Humphreys et al., 2006; Streck, 2008; Cashman & Blundy, 2013; Bennett et al., 2019; Mangler et al., 2024](#)). Experimental work has found that skeletal growth of feldspar may be caused by undercooling, and that typically during undercooling feldspar compositions are more sodic ([Bennett et al., 2019](#)). Conversely, feldspar dissolution features have been found to be associated with changes in liquid compositions, temperature, and pH_2O (volatile pressure) ([Nakamura & Shimakita, 1998; Humphreys et al., 2006; Cashman & Blundy, 2013; Bennett et al., 2019; Mangler et al., 2024](#)).

Compaction microstructures

Compaction of a crystal mush may occur over a range of crystallinities (e.g. [Philpotts & Philpotts, 2005; Florez et al., 2024](#)). Thus, the timing of compaction is important as this may affect which mineral phases deform or rotate. For example, if compaction ceases while interstitial minerals are crystallising, there may be a final, undeformed interstitial component that reflects growth after compaction stops (e.g. [Holness et al., 2017](#)). Depending on the mush crystallinity, crystal shape, and crystal size, compaction will occur either via: (1) mechanical compaction through crystal repacking, rotation, and rearrangement, or (2) viscous grain deformation (i.e. compaction via dislocation creep, dissolution–precipitation creep, or diffusion creep) (e.g. [Torquato et al., 2000; Gray et al., 2003; Donev et al., 2004; Philpotts & Philpotts, 2005; Holness et al., 2017; Bachmann & Huber, 2019; Vukmanovic et al., 2019](#)). Mechanical compaction can occur simultaneously with the removal of interstitial liquid, or during liquid–mush flow during shearing/slumping of the crystal pile ([Meurer & Boudreau, 1996, 1998b, 1998a; O'Driscoll et al., 2007, 2008; Higgins, 2011; Holness et al., 2017](#)). Textural evidence of mechanical compaction includes crystal tiling or draping of undeformed crystals around other grains, particularly where larger crystals restrict the movement of smaller crystals, and possibly the development of a shape preferred orientation (Fig. 1e) ([Philpotts & Philpotts, 2005](#)). For example, 'intel structures' may be observed, where larger crystals support overlying sinking crystals, and trap liquid rising from below (Fig. 1e) ([Philpotts & Philpotts, 2005](#)). We note that cooling rates contribute to the development of these textures, as slower cooling rates provide more time for crystal accumulation to occur ([Philpotts & Philpotts, 2005](#)). Critically, during mechanical compaction there is little plastic deformation, with only minor bending or breaking of larger crystals if they form intel structures ([Nicolas, 1992; Philpotts & Philpotts, 2005; Holness et al., 2017](#)).

Compaction via viscous grain deformation generally occurs once the crystal framework reaches its maximum packing fraction, as the weight of the overlying pile causes crystals to deform plastically as they cannot move or rotate (e.g. [Bachmann & Huber, 2019; Florez et al., 2024](#)). However, some argue that compaction via viscous grain deformation may occur even before the maximum packing fraction is reached, while high liquid fractions are still present ([Connolly & Schmidt, 2022](#)). The processes enabling

this viscous grain deformation are dislocation creep, dissolution–precipitation, and/or diffusion creep ([Cooper & Kohlstedt, 1984; Tullis & Yund, 1991; Hirth & Tullis, 1992; Hirth & Kohlstedt, 1995; Rosenberg, 2001; Mei et al., 2002; Scott & Kohlstedt, 2006; Svahnberg & Piazzolo, 2010; Lee et al., 2022](#)). Dislocation creep involves the formation of linear crystal lattice defects, i.e. dislocations, that move, accumulate, and rearrange to form low-energy configurations (e.g. [Paterson, 2001; Vernon, 2004; Cross & Skemer, 2019](#)). Microstructurally this is expressed by crystal lattice bending, i.e. undulose extinction, kink bands, deformation twinning, presence of sub-grains, and/or new small grains (recrystallisation) (Fig. 1f) (e.g. [Guillope & Poirier, 1979; Drury & Urai, 1990; Nicolas, 1992; Vernon, 2004](#)). Additionally, compaction via dislocation creep may promote development of a crystallographic preferred orientation (CPO) if strains are high enough; this originates from the preference of particular slip systems active during dislocation creep at certain conditions (e.g. [Ji & Mainprice, 1990; Law, 1990; Stünitz et al., 2003; Svahnberg & Piazzolo, 2010](#)). Alternatively, compaction may be accommodated through diffusive mass transport processes such as diffusion or dissolution–precipitation creep at high-stress sites ([Cooper & Kohlstedt, 1984; Meurer & Boudreau, 1998a; Paterson, 2001; Rosenberg, 2001; Svahnberg & Piazzolo, 2013; Holness et al., 2017](#)). Diffusion creep is a stress-induced solid-state diffusion of vacancies through a crystal lattice or along grain boundaries, whereas dissolution–precipitation requires a fluid in which elements are transported from high-stress to low-stress sites along a chemical gradient ([Rutter, 1983; Vernon, 2004; Lee et al., 2022](#)). Microstructural evidence of diffusion creep and dissolution–precipitation includes asymmetric compositional overgrowths on crystal faces in low-stress orientations, the truncation of grains at high-stress sites, and grain interpenetration with sutured contacts (Fig. 1g) ([Rosenberg, 2001; Svahnberg & Piazzolo, 2010, 2013; Stünitz et al., 2020](#)). Importantly, experimental work shows similar microstructural indicators as compaction via dissolution–precipitation may form during chemically induced dissolution–precipitation reactions without any differential stress ([Putnis, 2009; Spruzeniec et al., 2017](#)). To distinguish between microstructures that form due to deformation rather than exclusively by chemical disequilibrium, it is essential to consider the relationship between the microstructures formed and expected axes of maximum and minimum stress (e.g. during compaction the main stress axis is expected to be vertical). In addition, during chemically driven replacement reactions, the newly grown mineral commonly exhibits slight orientation changes (i.e. internal misorientations, contrasting with the undeformed, original grains) ([Spruzeniec et al., 2017](#)).

Microstructure modification

A common concern within microstructural studies is that early microstructures are modified or overprinted (e.g. [Glazner & Boudreau, 2011; Higgins, 2011; Holness & Vernon, 2015; Bartley et al., 2018; Holness et al., 2018](#)). Modification of early microstructures may result from two overarching processes: (1) textural equilibration during maintained high temperatures or low degrees of undercooling, or (2) dynamic recrystallisation following plastic deformation in a solid (e.g. [Holness, 2005, 2007, 2018; Passchier & Trouw, 2005; Vernon & Paterson, 2008](#)). Dynamic recrystallisation of highly strained grains may remove evidence of bent grains, however it should be noted that for significant dynamic recrystallisation to occur, stresses and finite strain must be relatively high ([Urai et al., 1986; Boorman et al., 2004; Rybacki & Dresen, 2004; Bachmann & Huber, 2019](#)). For example, at temperatures of 500 °C and grain sizes of 100 µm, differential

stresses would need to be 10–100 MPa for feldspar to recrystallise (Rybacki & Dresen, 2004). CPO can be used to assess whether a modified texture resulted from textural equilibration or dynamic recrystallisation, as recrystallised grains will preserve a strong CPO that corresponds to the dominant dislocation slip system (i.e. dislocation creep occurs along preferred crystal planes and axes for a particular mineral phase) (Lister & Hobbs, 1980; Law, 1990; Satsukawa *et al.*, 2013).

As an igneous rock cools under sub-solidus conditions, modification of earlier microstructures may produce a granular texture due to the minimisation of interfacial energies, where minerals have a relatively uniform shape and size, curvilinear grain boundaries, and $\sim 120^\circ$ three-grain junctions (when all three grains are the same phase) (Fig. 1h) (e.g. Vernon, 1968; Holness, 2005, 2007; Holness *et al.*, 2005; Leuthold *et al.*, 2014; Holness & Vernon, 2015; Holness & Fowler, 2022). In contrast to 120° three-grain junctions that develop in minerals with isotropic surface energies (e.g. quartz, nepheline, sodalite), textural modification involving minerals with highly anisotropic surface energies (e.g. amphibole), grain boundary adjustment produces a texture characterised by three-grain junctions $<120^\circ$ (Fig. 1i) (Bons *et al.*, 2001; Piazzolo *et al.*, 2016).

GEOLOGICAL BACKGROUND

Geological setting

The Ilímaussaq complex (1160 ± 5 Ma) is part of the Gardar igneous province of South Greenland, which formed during two discrete rifting events associated with the breakup of the Columbia/Nuna supercontinent between 1300 and 1100 Ma (e.g. Upton *et al.*, 2003; Krumrei *et al.*, 2006; Upton, 2013; Borst *et al.*, 2019). The Ilímaussaq complex was emplaced between the granitic Julianehåb batholith (c. 1800 Ma) and overlying sandstones and basalts of the Eriksfjord Formation (c. 1300–1270 Ma) at ~ 3 –4 km depth (e.g. Garde *et al.*, 2002; Krumrei *et al.*, 2006; Upton, 2013). Ilímaussaq is an optimal natural laboratory for primary alkaline magmatic processes as it has ~ 1500 m of vertical exposure and no evidence of significant post-emplacement deformation (Andersen *et al.*, 1981; Upton *et al.*, 2003; Upton, 2013).

Ilímaussaq was formed through four intrusive phases of peralkaline to alkaline melt (e.g. Larsen & Sørensen, 1987; Sørensen, 2001; Sørensen *et al.*, 2006; Borst *et al.*, 2018). The first phase comprises augite syenite that is preserved around the margins and roof of the complex, followed by a second phase comprising alkali granite and quartz syenite preserved in the roof of the complex (Fig. 2a) (e.g. Sørensen, 2001). The third and fourth phases comprise the volumetrically dominant nepheline syenites that make up the roof, and floor, and ‘sandwich’ horizons (Fig. 2a) (e.g. Sørensen, 2001; Sørensen *et al.*, 2006; Pfaff *et al.*, 2008; Ratschbacher *et al.*, 2015; Borst *et al.*, 2018). The focus of our study is the floor horizon, locally referred to as kakortokite, as it displays well-defined macrorhythmic igneous layering and evidence of compaction which is described below.

General characteristics of kakortokite layered sequence

The base of the kakortokite sequence (i.e. the lower layered kakortokites) is >220 m thick and contains the best defined layering (Fig. 2c) (e.g. Bohse *et al.*, 1971; Marks & Markl, 2015). The igneous layering comprises a repeating ~ 8 -m-thick three-layer unit (Bohse *et al.*, 1971). The three layers are a basal black (B) arfvedsonite-rich layer, a central red (R) eudialyte-rich layer, and a top white (W) alkali feldspar- and nepheline-rich layer. Occasionally the red

layer is poorly developed or missing (Bohse *et al.*, 1971). These three-layer units are repeated a minimum of 29 times vertically through the kakortokite sequence (Fig. 2c) (e.g. Bohse *et al.*, 1971; Sørensen, 2001; Marks & Markl, 2015). The clearest three-layer unit is referred to as Unit 0, with the rest of the units labelled from -11 to $+17$ depending on their stratigraphic relationship relative to Unit 0 (Fig. 2c) (Bohse *et al.*, 1971).

Peralkaline melt characteristics and layer formation in the kakortokites

A limited number of experimental studies have examined peralkaline melts and their crystalline products (e.g. eudialyte, nepheline, arfvedsonite), so a thermodynamic model for a hydrous peralkaline system, such as Ilímaussaq, has yet to be produced (Giehl *et al.*, 2013, 2014; Nikolenko *et al.*, 2024; Weller *et al.*, 2024). However, the interval between the liquidus and solidus of the kakortokite peralkaline melt is known to cover an extended temperature range, with nepheline, Na-pyroxene, albite equilibria indicating temperatures of ~ 800 – 700°C at silica activities ~ 0.5 – 0.3 , and $\sim 500^\circ\text{C}$ at silica activities ~ 0.25 (Markl *et al.*, 2001). This extended crystallisation period is considered to result from high concentrations of alkalis (Na) and volatiles (Cl, F, H_2O) in the melt, which strongly influence phase stabilities, solidus temperatures, and viscosity (Piotrowski & Edgar, 1970; Sood & Edgar, 1970). Additionally, the peralkaline melt at Ilímaussaq is thought to have been saturated with multiple phases, with all major mineral phases appearing on the liquidus more or less contemporaneously (see Table 1 for an overview of the major minerals in the kakortokites) (Piotrowski & Edgar, 1970; Larsen, 1976, 1977; Larsen & Sørensen, 1987). Due to the highly variable nature of the phase stabilities and solidus temperatures, it is difficult to delineate a simple liquid line of descent or calculate expected cotectic proportions (Giehl *et al.*, 2013, 2014).

The highly volatile nature of the kakortokite peralkaline melt, and the associated uncertainty regarding the expected crystallisation sequence, has resulted in a wide variety of hypotheses for how modal layering in the kakortokites formed. Proposed layering hypotheses, mostly derived from eudialyte geochemical trends, include: (1) episodic convective overturns (Bohse *et al.*, 1971); (2) repeated magma recharge and/or degassing (Pfaff *et al.*, 2008; Hunt *et al.*, 2017); (3) crystallisation of a compositionally stratified magma reservoir (Larsen & Sørensen, 1987); (4) fluctuations in intensive parameters such as temperature, vapour pressure, or volatiles, resulting in alternating crystallisation of major mineral phases (Larsen & Sørensen, 1987; Pfaff *et al.*, 2008; Hunt *et al.*, 2017); and (5) the formation of crystal mats through density segregation and gravitational settling (Bons *et al.*, 2015; Lindhuber *et al.*, 2015; Borst *et al.*, 2018).

A lack of magma flow fabrics and consistent mineral foliations identified in recent textural studies of the Ilímaussaq kakortokites suggest gravitational settling was an important process during layer formation, favouring the latter crystal mat hypothesis (O'Driscoll *et al.*, 2024; Jones *et al.*, 2025). In the crystal mat model, all major mineral phases nucleate contemporaneously below a rising crystallisation front. As the minerals grow, denser minerals (e.g. arfvedsonite) sink, while less dense minerals (e.g. alkali feldspar) float. With continued crystallisation, larger, heavier minerals catch up with lighter, smaller minerals, and loosely aggregated crystal mats begin to form via hindered settling. The crystal mats develop progressively from the bottom of the magma reservoir up with the rising crystallisation front. Further crystallisation within the crystal mats forms semi-permeable mush compartments, within which liquid fractionation and gravitational

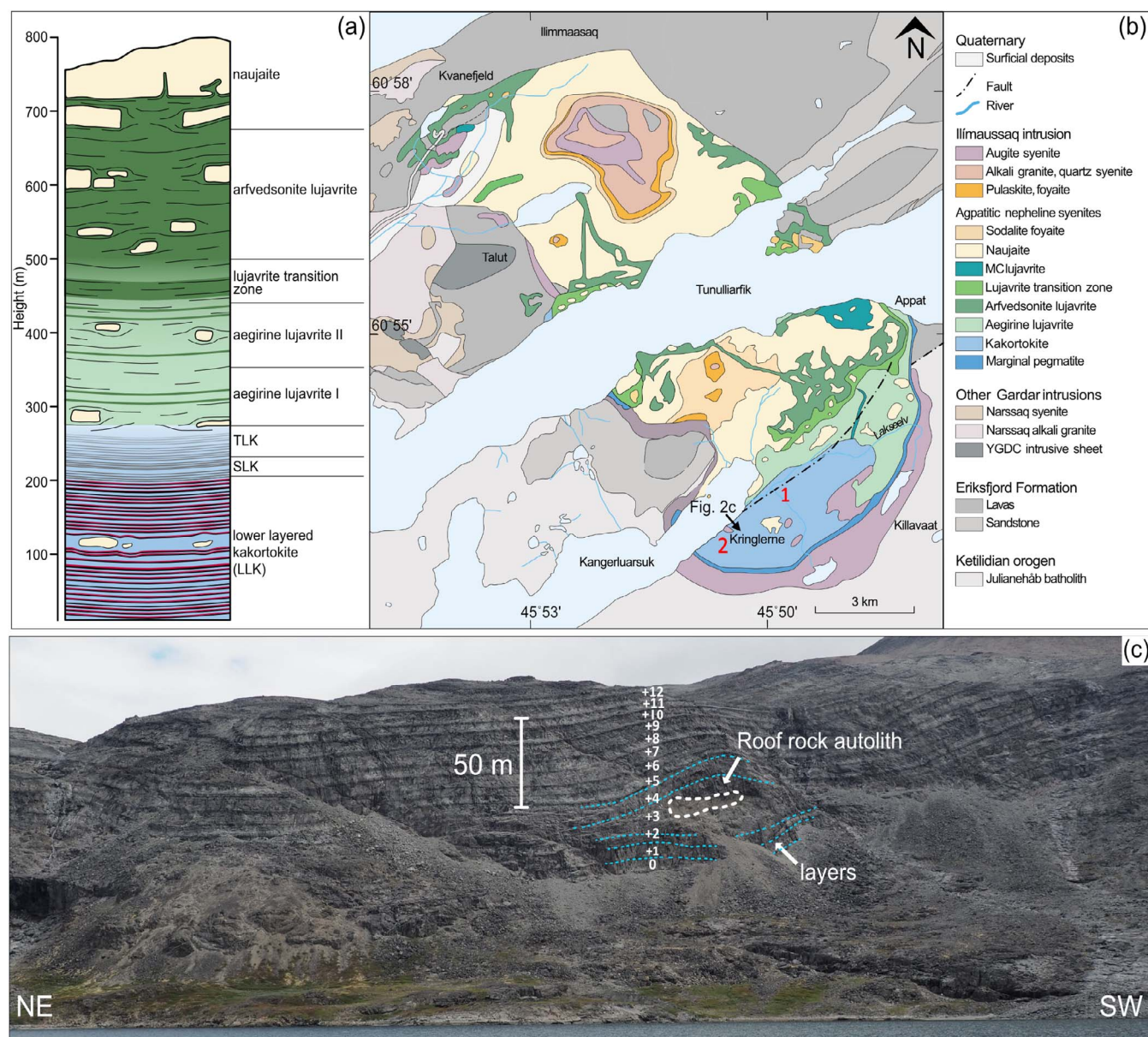


Fig. 2. General geology of the Ilímaussaq complex modified from Jones *et al.* (2025). (a) Schematic cross-section through the Ilímaussaq complex modified from Andersen *et al.* (1981); (b) geological map of the Ilímaussaq complex adapted from Upton (2013). Locations of study sites are labelled '1' and '2'; (c) photograph of the lower layered kakortokites with units 0 to +12 labelled. Dotted white outline highlights roof rock autolith with layers wrapping around it.

settling further segregate arfvedsonite, eudialyte, nepheline, and alkali feldspar into layered horizons.

Fabrics in the kakortokites: recent observations and interpretations

Recent field, rock magnetic, and electron backscatter diffraction (EBSD) fabric studies of the kakortokites report a consistent sub-horizontal foliation defined by silicate minerals (i.e. orthoclase and arfvedsonite), and a sub-horizontal and sub-vertical foliation, commonly orthogonal to igneous layering, defined by magnetite (O'Driscoll *et al.*, 2024; Jones *et al.*, 2025). Critically, this silicate mineral foliation is commonly oblique to the attitude of the inclined modal igneous layering, which is attributed to differential mechanical compaction during roof rock autolith collapse and subsequent intrusion-wide mechanical compaction (Fig. 3) (Jones *et al.*, 2025). The sub-vertical magnetite fabric, measured using

anisotropy of anhysteretic remanence (AARM), which reflects the long axis alignment of magnetite only, may record vertical migration of interstitial liquid across igneous layers (Jones *et al.*, 2025). The presence of three distinct fabrics (i.e. modal layer attitude, silicate mineral foliation, and magnetite foliation) that are oblique to one another suggests that at least one post-cumulus process significantly affected the kakortokites, making them an ideal study location for investigating crystal-melt separation mechanisms.

SAMPLING AND ANALYTICAL METHODS

Sampling and study site description

A total of 21 representative samples were selected from two localities where igneous layering is well defined in outcrop (Figs 2b and 4a, b). Twelve samples (numbers 64, 65, 66, 68, 69, 71, 75, 77, 79, 83, 85, and 90) were selected from Locality 1 layers -1W to +1B

Table 1: Summary of the main minerals that define the modal layering at Ilímaussaq (see Peterson, 2001 and references therein)

Mineral phase	Chemical formula	Density (g/cm ³)
Arfvedsonite	Na ₃ (Fe ²⁺ ,Mg) ₄ Fe ³⁺ Si ₈ O ₂₂ (OH) ₂	3.3–3.5
Eudialyte	Na ₁₅ Ca ₆ Fe ₃ Zr ₃ Si(Si ₂₅ O ₇₃)(O,OH,H ₂ O) ₃ (Cl,OH) ₂	2.74–3.1
Nepheline	(Na,K)AlSiO ₄	2.55–2.66
Alkali feldspar	(Na,K)AlSi ₃ O ₈	2.55–2.63

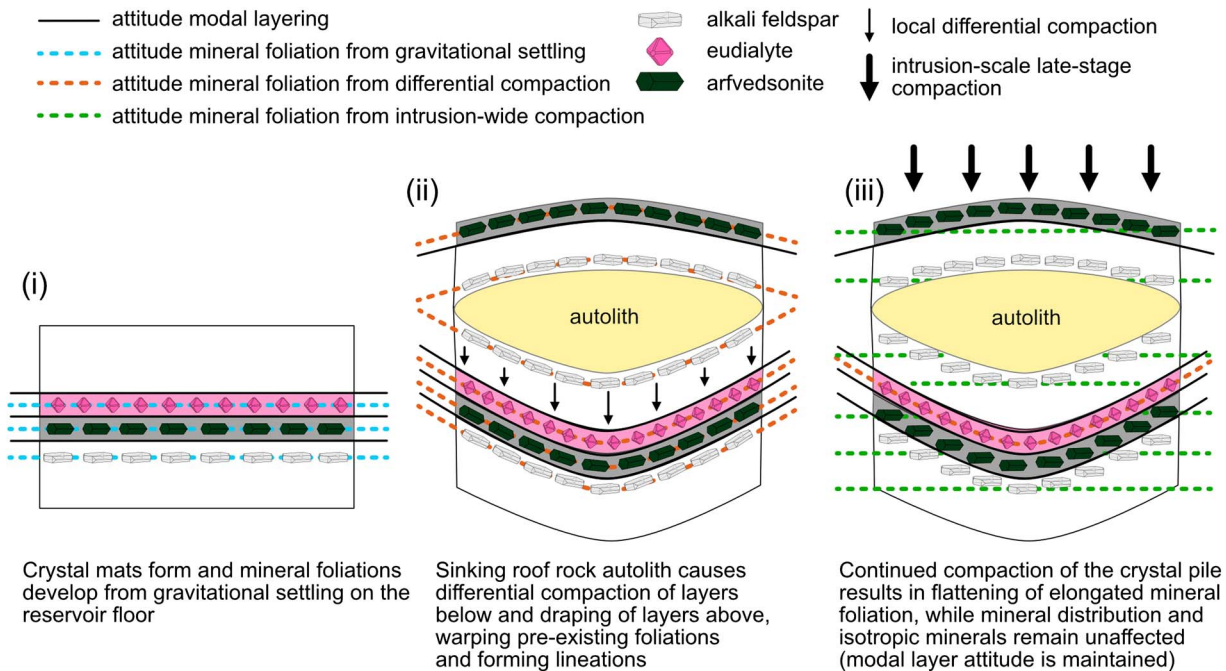


Fig. 3. Schematic diagram of the development of silicate mineral fabrics within the kakortokites as proposed by Jones *et al.* (2025).

(Fig. 4a) and nine samples from Locality 2 (numbers 11, 12, 15, 17, 20, 23, 24, 27, and 29) layers 0 W to +2 W (Fig. 4b). Samples were collected from the base to the top of the three-layer units to assess how textures varied vertically through the stratigraphy. Samples with varying proportions of interstitial to primocryst minerals were selected to examine how microstructures change with different interstitial liquid abundances. Samples were collected using a handheld drill with a 25-mm-diameter drill bit and were drilled normal to layering. A Pomeroy orientating fixture was used to measure core orientations and sample locations were recorded using a GPS and on 1:100 scale window maps.

Petrography and quantitative crystallographic orientation analysis (EBSD) combined with chemical analysis (EDS)

Twenty-one polished thin sections were prepared from oriented core samples to examine mineral textures and microstructures. Thin sections were cut normal to igneous layering from drill core samples (i.e. the top of all thin sections represents the way up in igneous layering). Seven representative polished thin sections were selected for EBSD analysis to measure mineral modal abundances and whole thin section CPO of main phases, while detailed microstructural analyses were undertaken to assess chemical reaction textures and deformation features. EBSD was completed at the University of Leeds on an FEI Quanta 650 FEG-ESEM with AZtec software and an Oxford Symmetry EBSD detector. Energy dispersive spectroscopy (EDS) data was collected to confirm the mineral phases identified by EBSD and to assess any zoning within

the minerals. Acquisition settings were 30 kV, 27 mm working distance, and 70° specimen tilt. Step sizes of 5–15 µm were used for larger EBSD maps covering ~10 mm² of the thin section, and step sizes of 2–4 µm were used for detailed EBSD maps. Automatic indexing of arfvedsonite, eudialyte, nepheline, orthoclase, albite, aegirine, sodalite, and fluorite was completed using the AZtec software (Oxford Instruments) and AZtecCrystal v 6.1 (Oxford Instruments) was used to complete standard noise reduction, pole figures, inverse pole figure maps (IPF maps), and grain reference orientation deviation (GROD) angle maps.

Definition of microstructural types and microstructural types statistics

Full thin section crossed polarised light photomosaics were collected using a VHX digital microscope (see Supplementary material). The photomosaics were then used to identify general characteristics of microstructures associated with textural modification, deformation, chemical disequilibrium, and liquid-related growth including: (1) grain boundary and junction geometries; (2) kinking and breaking; (3) zoning patterns; (4) dissolution and replacement; and (5) microcrystic grains. The following microstructures were then counted across the entirety of each photomosaic: curvilinear grain boundaries, irregular (i.e. undulating/wavy) grain boundaries, apparent 120° three-grain junctions, kinking/breaking, overgrowth zoning, mineral dissolution, albite replacement, impact nucleation, and glomerocrysts. Impact nucleation is a new term that we define and describes the clusters of microcrystic (<50 µm) albite that nucleated and grew at high-angle intersections of

alkali feldspar laths. Photomosaics with each of these microstructures circled are included in the Supplementary material. For mineral replacement microstructures that are patchy across a single mineral, one occurrence of the replacement microstructure was counted per crystal. For grain boundary microstructures, one microstructure was counted per grain boundary of a single crystal. Interstitial minerals were identified as anhedral minerals occupying the pore spaces between euhedral primocryst minerals.

RESULTS

General characteristics: phase proportions, grain size, and grain shapes

Black layers

Black layers are dominated (55–65%) by subhedral arfvedsonite (Fig. 5a and d). In layer 0B the arfvedsonite is relatively fine-grained (<1–2 mm) and in layers +1B and +2B the arfvedsonite is coarser grained (~2–3 mm) (images of layers +1B and +2B are provided in the Supplementary material). Alkali feldspar (15–25%) is coarse (3–8 mm) and has an elongate, euhedral shape and straight grain boundaries (Fig. 5a); in layer 0B, towards the contact with layer –1W, rare skeletal albite is observed (Fig. 5j). Nepheline (5–15%) and eudialyte (5%) are subhedral to anhedral (Figs 5a and 6b, h). Sodalite and fluorite are minor (<5%), subhedral to anhedral, and typically fill pore spaces between arfvedsonite grains (Fig. 6g), but also rarely present as euhedral phases (see Supplementary material). Rare aenigmatite is present (<1%) in either a euhedral form or as inclusions within arfvedsonite grains (see Supplementary material).

Red layers

Red layers are dominated by euhedral eudialyte (20–65%) and alkali feldspar (15–50%) (Fig. 5b and e). Eudialyte always has straight grain boundaries and a consistent grain size of ~3 mm (Fig. 5b and e). Alkali feldspar (~3–8 mm) is mostly elongate and euhedral, but commonly shows impingement textures with adjacent eudialyte; e.g. alkali feldspar grain boundaries wrapping around adjacent eudialyte (Fig. 5e). Nepheline (10–20%) is typically subhedral, with impingement textures with surrounding alkali feldspar and eudialyte (Fig. 5e). Arfvedsonite and aegirine together make up 20–35% and typically have straight grain boundaries defined by the surrounding cumulus grains (Fig. 5b and e). Rare aenigmatite is present (<1%) typically as inclusions within arfvedsonite and aegirine (see Supplementary material).

White layers

White layers are dominated by euhedral alkali feldspar (60–65%) (Fig. 5c and f), except for the bottom half of layer 0W, which is dominated by nepheline (35–65%) and alkali feldspar (15–50%) (Figs 5h and 6d, e). The bottom half of layer 0W also contains eudialyte (5–15%) with oikocrysts of arfvedsonite, aegirine, sodalite, and fluorite (Figs 5h and 6e). Within these oikocrysts are nepheline chadacrysts, which vary in size (1–4 mm), have irregular grain boundaries, and display no clear size distribution (Figs 5h and 6f). Nepheline (1–4 mm) outside the oikocrysts is typically subhedral, showing impingement textures with surrounding nepheline and eudialyte grains (Fig. 6d and e). Alkali feldspar (3–10 mm) is elongate and euhedral (Fig. 5h), and eudialyte (~3 mm) is typically subhedral with curvilinear grain boundaries that fill in spaces between adjacent nepheline grains (Fig. 6e). Rare skeletal albite is recorded (see Supplementary material).

The top of layer 0W, and layers –1W, +1W, and +2W contain coarse alkali feldspar (8–15 mm), nepheline (15–25%), eudialyte

(5%), and sodalite/fluorite (<5%) with arfvedsonite/aegirine (10–20%) (Fig. 5c and f). Alkali feldspar (3–10 mm) is elongate and euhedral with straight grain boundaries (Fig. 5c and f). Nepheline (1–4 mm) is typically euhedral to subhedral with impingement textures with adjacent nepheline, alkali feldspar, and eudialyte (Fig. 5f and g). Eudialyte (~3 mm) is typically euhedral with straight grain boundaries (Fig. 5k and l). Arfvedsonite and aegirine are euhedral to anhedral, with straight grain boundaries typically defined by the surrounding minerals (Fig. 5g).

Identified microstructural types

The following microstructural features have been identified across our samples: (1) textural modification microstructures (e.g. curvilinear grain boundaries, apparent 120° three-grain junctions); (2) deformation microstructures (e.g. mineral bending, mineral breaking, impact nucleation); (3) chemical disequilibrium microstructures (e.g. irregular grain boundaries, eudialyte overgrowth zoning, mineral dissolution, albite replacement); and (4) liquid microstructures (e.g. impact nucleation, glomerocrysts). While microstructural types were identified using optical microscopy, we further quantitatively characterised the microstructural types using EBSD combined with EDS. Here we will provide examples of each microstructure type and where they are identified within the three-layer units.

Textural modification: grain boundaries and three-grain junctions

In black layers arfvedsonite, nepheline, and eudialyte typically have curvilinear grain boundaries, particularly when in contact with other arfvedsonite grains (Figs 5d and 6a–c, g–h). Eudialyte, fluorite, and sodalite occasionally have apophyses that extend around adjacent arfvedsonite (note maintained orientation of fluorite, Fig. 6g and h), and rare three-grain arfvedsonite junctions with apparent dihedral angles of 120° are also recorded in black layers (Figs 5a and 6a). In red and white layers, curvilinear boundaries are rare to absent, except for nepheline–nepheline grain boundaries at the base of layer 0W (Fig. 6e). Irregular grain boundaries (i.e. wavy, undulose on the micrometre scale) are commonly observed in red and white layers, particularly at the contacts between nepheline and oikocrystic arfvedsonite (Fig. 6d and f) or aegirine (see Supplementary material). No irregular grain boundaries are observed in black layers.

Deformation microstructures

Deformation microstructures associated with dislocation creep are rarely observed within our samples. No undulose extinction, sub-grains, or mechanical twinning are recorded within any of the samples (see lack of misorientation within nepheline ground-mass, Fig. 7ciii and civ). Towards the top of the white layers, alkali feldspar laths are occasionally broken (Fig. 7a), bent (Fig. 7b–d), or have microcracks (Fig. 7e) where they are in contact with other grains. Of particular note is that breaking/bending of alkali feldspar is always associated with the presence of albite (Fig. 7). Patchy orthoclase within alkali feldspar is mostly undeformed (Fig. 7ciii), whereas albite surrounding the orthoclase has misorientation angles ~5° (Fig. 7civ). Minerals surrounding deformed alkali feldspar grains are undeformed (Fig. 7ciii and civ).

Chemical disequilibrium: mineral zoning and replacement

Arfvedsonite is commonly zoned across all studied layers. Most of the arfvedsonite has a patchy zoning with an irregular core in the centre of the grain (Fig. 8a). Rarely, in layer 0B zoning within arfvedsonite occurs preferentially along grain boundaries

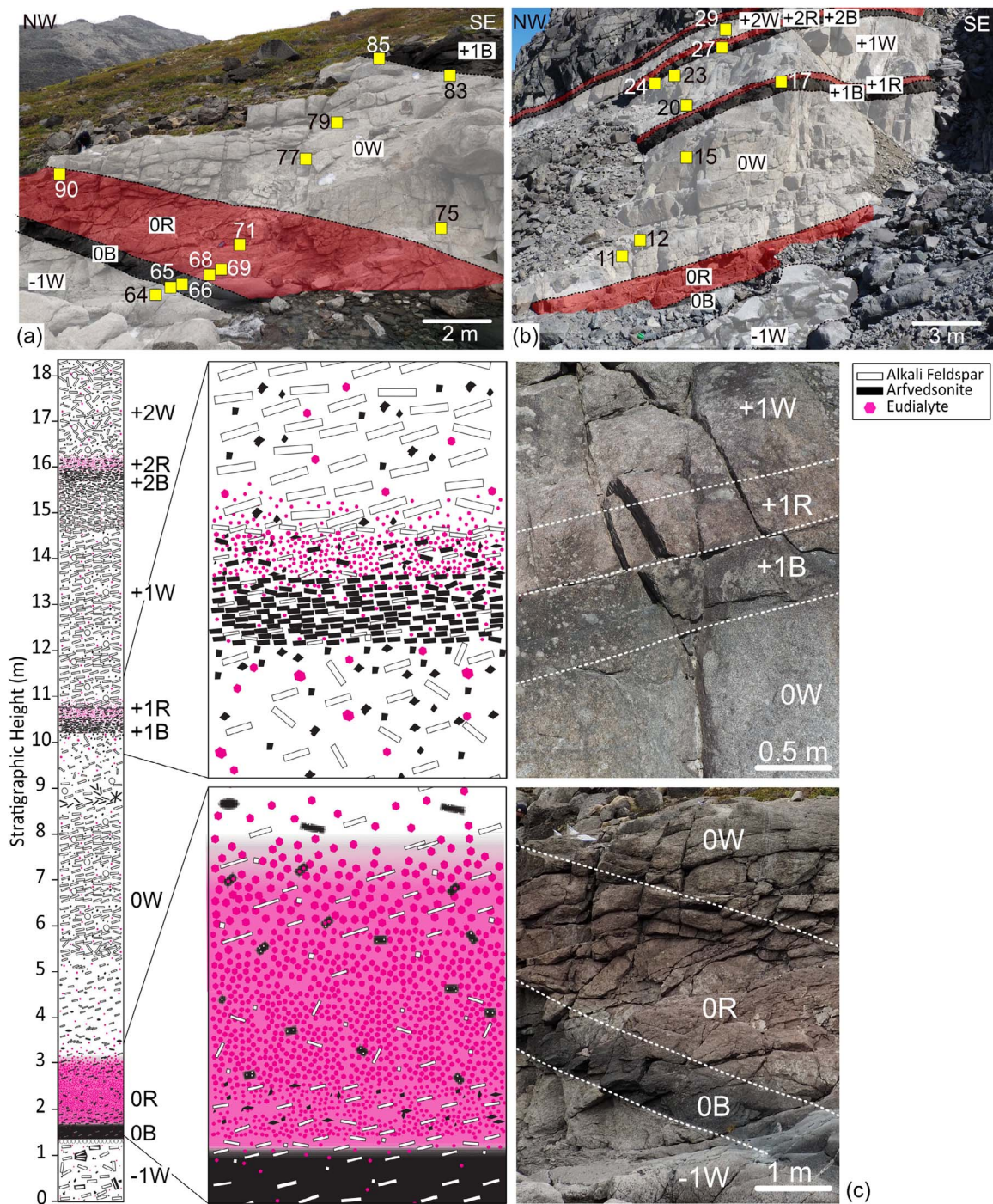


Fig. 4. Schematic textural log and sample locations across layers -1W to +2W of the kakortokites. (a) and (b) Localities 1 and 2, respectively, with sample locations highlighted with boxes, and modal layering annotations. (c) Stratigraphic log from Jones *et al.* (2025) recording textures from layers -1W to +2W at Locality 2. Zoomed-in sections of the log highlight differences between the well-developed layers of Unit 0 versus the poorly developed layers of Unit +1, as well as the oblique relationship between the alkali feldspar foliation and modal igneous layering. Note the much higher concentration of eudialyte in layer 0R compared to layers +1R and +2R. Adjacent to the highlighted log sections are the associated photographs of Units 0 and +1.

where the arfvedsonite is in contact with other arfvedsonite grains (Fig. 8b). Arfvedsonite zoning is defined by variations in Na/K and reflects the appearance of analcime as an interstitial mineral phase (Pfaff *et al.*, 2008). Almost all eudialyte has sector zoning (Fig. 8c and d); in white layers eudialyte typically has sector zoning in its centre, and overgrowth zoning around the grain edges (Fig. 8c and d). The overgrowth zoning occurs in both euhedral and subhedral eudialyte (Fig. 8c and d).

Across all studied layers, alkali feldspar has microstructures that we attribute to fluid-mediated, interface-coupled mineral replacement due to its patchy nature and local compositional variation between albite and orthoclase (Fig. 5f, i and l) (Putnis, 2009; Schønwandt *et al.*, 2023). The centre of alkali feldspar typically exhibits a patch perthite texture, surrounded by an albite periphery (Figs 8f, h and 9a–c). Albite and orthoclase show epitaxy (see similar orientation of 3-D unit cells, Fig. 8f). Albite replace-

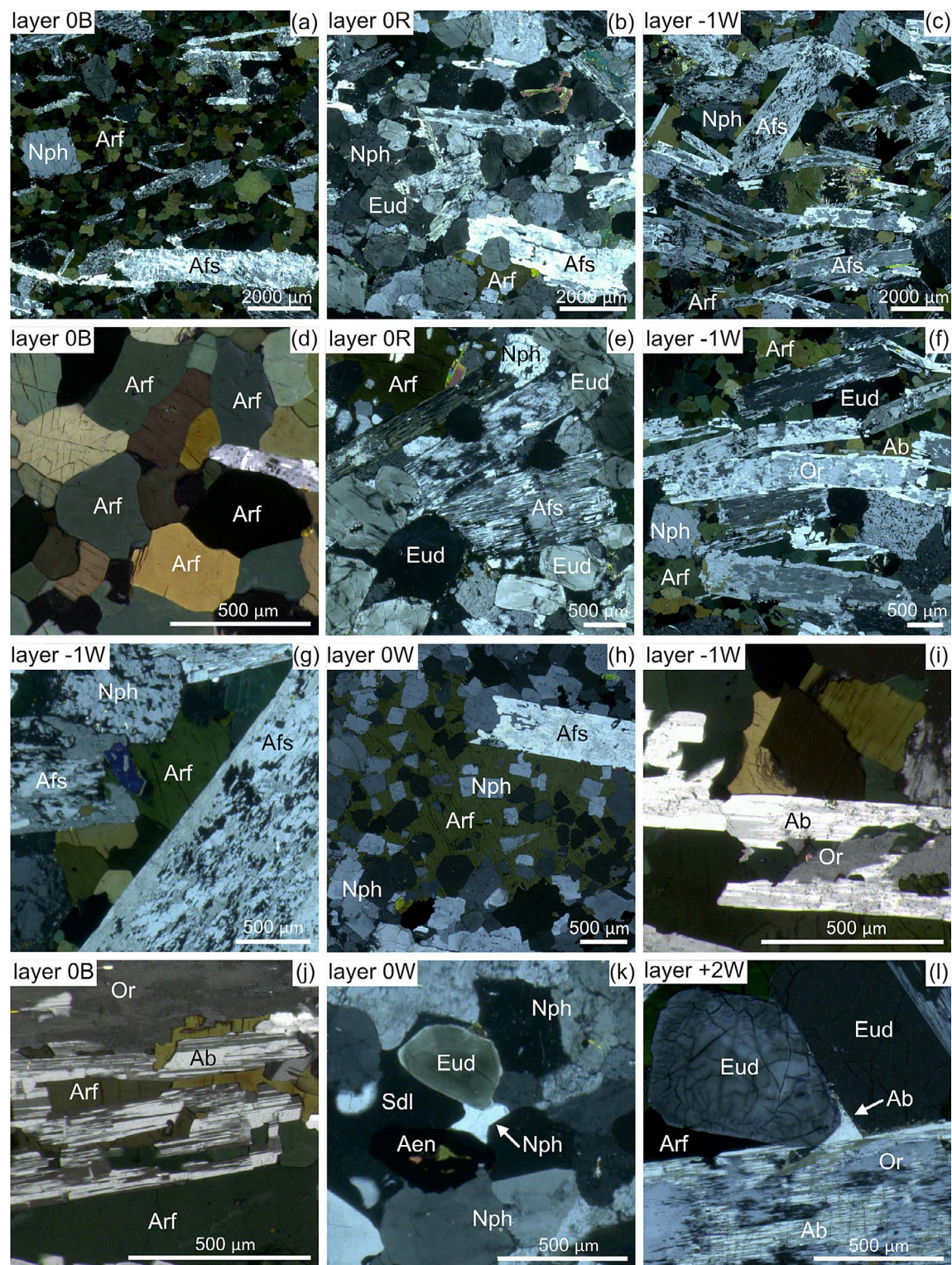


Fig. 5. Cross-polarised thin-section images of general characteristics of layers in the kakortokites. Nph, nepheline; Arf, arfvedsonite; Afs, alkali feldspar; Eud, eudialyte; Or, orthoclase; Ab, albite; Sdl, sodalite; Aen, aenigmatite. (a) Layer 0B with fine-grained arfvedsonite matrix with alkali feldspar laths; (b) Layer 0R with abundant eudialyte and impingement textures between eudialyte and alkali feldspar; (c) Layer -1W with coarse alkali feldspar laths and strong fabric; (d) Arfvedsonite in layer 0B; (e) Impingement of alkali feldspar with eudialyte and nepheline in layer 0R; (f) Layer -1W with albitisation of alkali feldspar; (g) Interstitial arfvedsonite in layer -1W; (h) arfvedsonite oikocryst at base of layer 0W; (i) Albitisation of orthoclase in layer -1W; (j) Skeletal alkali feldspar at the base of layer 0B; (k) Interstitial nepheline occupying pore space between primocryst minerals; (l) Interstitial albite occupying pore space between primocryst minerals.

ment of orthoclase is increasingly more pervasive from the base to the top of a three-layer unit; in black layers albite is typically confined to a thin rim around the grain whereas in white layers

albite appears along the rims and central patches of the grains (Fig. 9a–c). The base of layer 0W records the most extensive albite replacement with nearly all orthoclase replaced by albite (Fig. 8f).

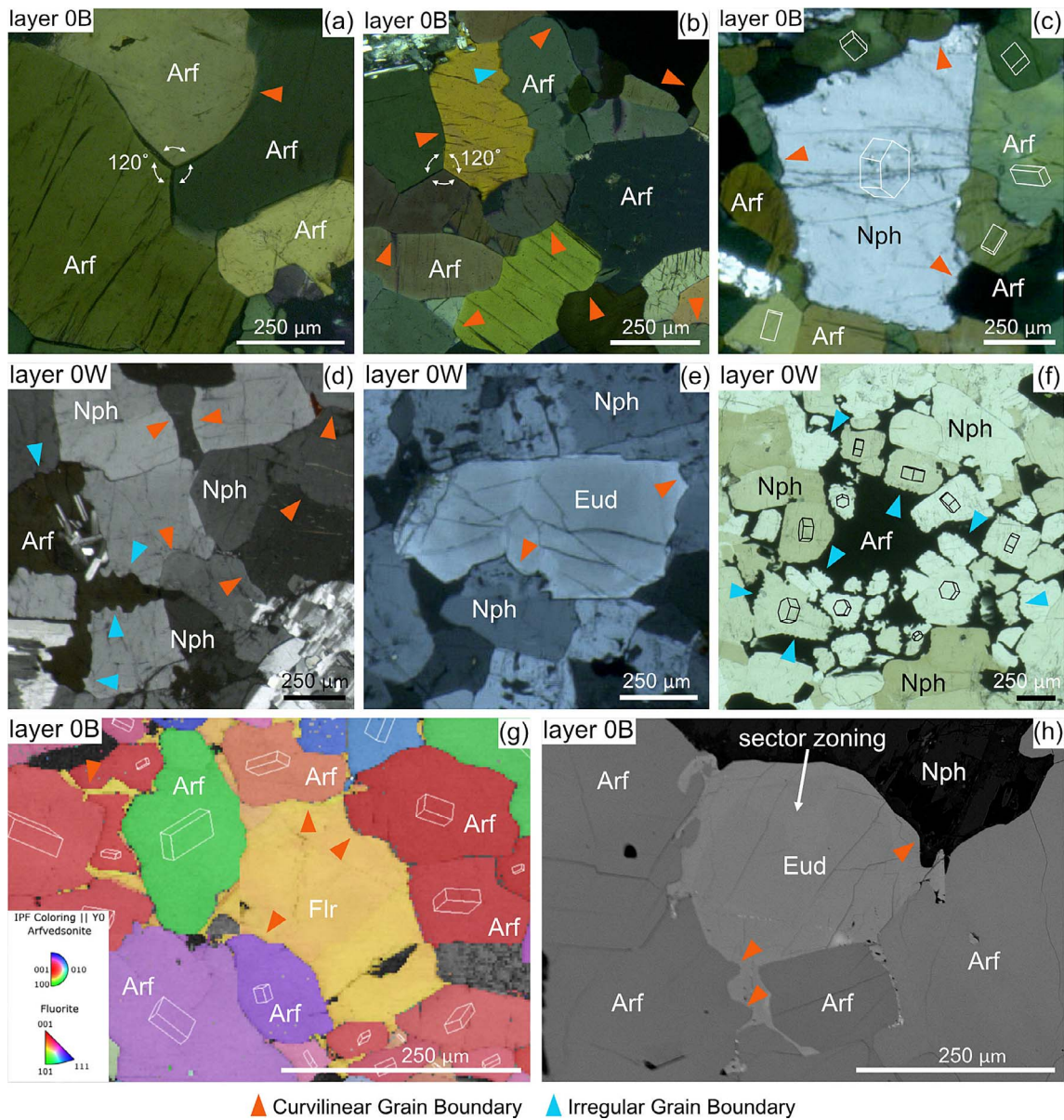


Fig. 6. Grain boundary and three-grain junction geometries in the kakortokites. Mineral abbreviations as in Fig. 4. (a) XPL thin-section image of apparent 120° junction between arfvedsonite; (b) XPL thin-section image of apparent 120° junction, curvilinear grain boundaries, and irregular grain boundaries between arfvedsonite; (c) XPL thin-section image of curvilinear grain boundaries with grain 3-D unit cells measured with EBSD in white; (d) XPL thin-section image of curvilinear and irregular grain boundaries at the base of layer 0 W; (e) XPL thin-section image of curvilinear grain boundaries towards base of layer 0 W; (f) PPL thin-section image of irregular grain boundaries within oikocrysts at base of layer 0 W. 3-D unit cells measured with EBSD in black; (g) EBSD IPF map of anhedral fluorite with extended apophyses around arfvedsonite (note maintained orientation of fluorite across apophyses and rounded nature of arfvedsonite). Arfvedsonite 3-D unit cells measured with EBSD in white; (h) BSE image of eudialyte with sector zoning in the core, extended apophyses, and new overgrowth rim.

In addition to albite replacement of orthoclase, arfvedsonite is commonly recorded as irregular patches within alkali feldspar grains (Figs 5i and 8g). Arfvedsonite within the alkali feldspar grains maintains the same crystallographic orientation as the rest of the arfvedsonite grain outside the alkali feldspar (Fig. 8g). This arfvedsonite growth into alkali feldspar occurs in black, red, and white layers; the replacement is more common in black layers where there is a higher abundance of arfvedsonite. At the base of layer 0W, occasionally nepheline rather than arfvedsonite is recorded growing within alkali feldspar.

Other minerals that show replacement textures are aenigmatite, nepheline, and arfvedsonite. Aenigmatite, nepheline, and arfvedsonite do not show any replacement textures in black

layers; however in red and white layers these minerals commonly are replaced (Fig. 5g, 8e & 8f). Aenigmatite typically is significantly replaced by aegirine (see similar orientation of 3-D unit cells, Fig. 8e), and arfvedsonite sometimes has a pothole texture formed by aegirine replacement (Fig. 8h, and see similar orientation of 3-D unit cells in Fig. 9a). Nepheline typically has a sieve texture due to sodalite replacement (Fig. 5g, and see similar orientation of 3-D unit cells in Fig. 8f).

Liquid: microcrystic grains

In white layers, small albite grains <<1 mm are frequently observed at the contacts between two alkali feldspar laths oriented at high (>45°) angles to one another (Fig. 9a–c).

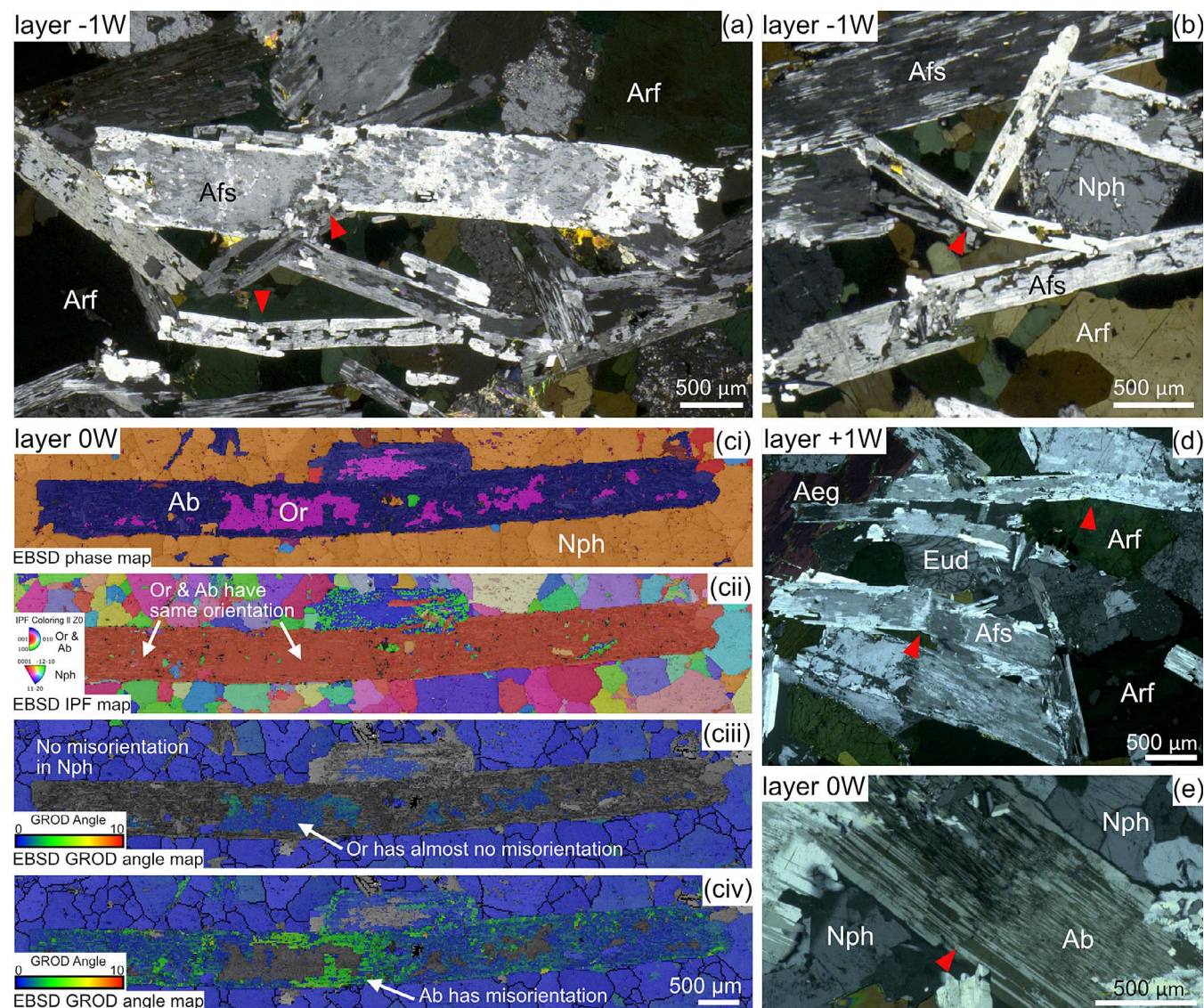


Fig. 7. Mineral breaking and bending in all images is highlighted with a red arrow. Aeg, aegirine; all other mineral abbreviations as in Fig. 4. (a) XPL thin-section image showing broken alkali feldspar; (b) XPL thin-section image showing bent alkali feldspar; (c) EBSD phase map of elongate alkali feldspar; (cii) EBSD IPF map showing similar orientation of orthoclase and albite; (ciii) EBSD GROD angle map of nepheline groundmass (showing no misorientation) and orthoclase with minimal misorientation; (civ) EBSD GROD angle map showing albite with misorientation; (d) XPL thin-section image showing bent alkali feldspar; (e) XPL thin-section image showing microcrack within alkali feldspar.

Here, albite is typically subhedral and twinning, if present, is polysynthetic, and no undulose extinction is observed (Fig. 9b and c). The orientation of the albite microcrysts displays some preferred orientation, similar to the orientation of the larger albite grain they are associated with (see pole figure, Fig. 9b).

A different type of microcrystic albite also appears in the form of glomerocrysts (Fig. 9d and e). The microcrystic albite within glomerocrysts are typically euhedral, elongate, have polysynthetic twinning, and are <1–2 mm in size (Fig. 9d and e). These albite grains form clusters where the minerals align with one another along their (010) faces (see pole figures, Fig. 9d and e). The albite glomerocrysts are identified within oikocrysts of various phases, as well as between primocryst phases (Fig. 9d and e). Arfvedsonite, fluorite, and aegirine oikocrysts maintain their orientation, showing 3-D connectivity around the chadacrysts (see consistent IPF colours across individual oikocrysts, Fig. 9d and e). Within the aegirine oikocryst there is a slight change in aegirine orientation

where it is in contact with albite crystals (see slight darkening of red IPF colouring, Fig. 9e).

Summary of microstructure distribution

A clear trend between mineralogy, grain size, and the proportion of interstitial material is evident across the layers (Fig. 10). Black layers are the finest grained and contain the lowest proportion of interstitial material (10–20%) (Figs 5a and 10). Grain size increases up through red and white layers, and the proportion of interstitial material is higher in red (20–35% interstitial) and white layers (20–40% interstitial) (Figs 5b, c and 10). Curvilinear grain boundaries and the number of apparent 120° three-grain junctions follow similar trends, peaking in black layers and the base of layer 0W (Fig. 10). An increase in curvilinear grain boundaries and the number of apparent 120° three-grain junctions coincide with either high arfvedsonite content, or high nepheline content (Fig. 10). The highest number of curvilinear grain boundaries and 120° three-grain junctions occurs in layer 0B, which is the finest grained

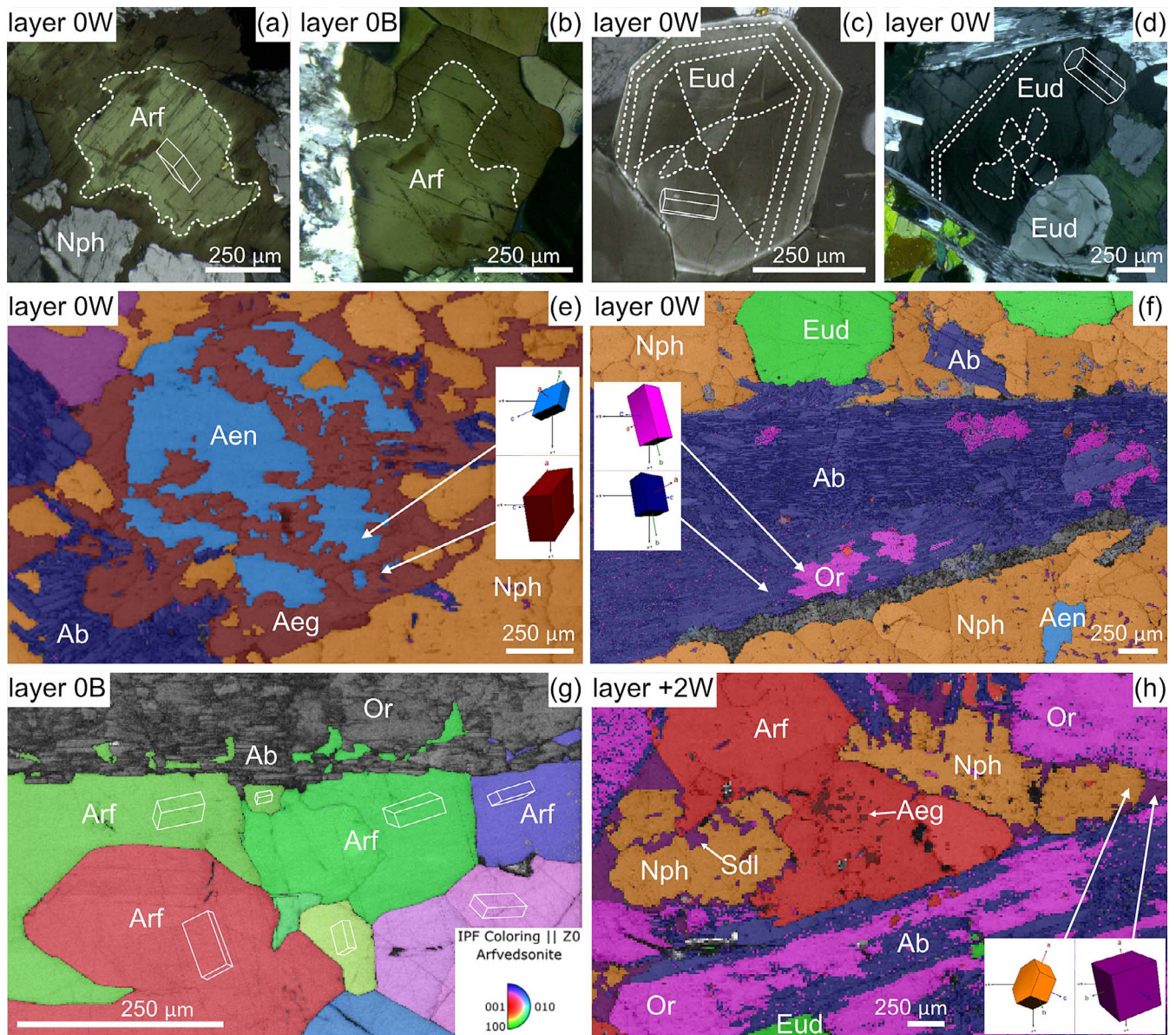


Fig. 8. Mineral zoning and replacement textures. Mineral abbreviations as in Figs 4 and 6. (a) XPL thin-section image showing patchy zoning of arfvedsonite. Arfvedsonite 3-D unit cell measured with EBSD in solid white; (b) XPL thin-section image showing preferential zoning of arfvedsonite where it is in contact with other arfvedsonite grains; (c) XPL thin-section image showing euhedral eudialyte with sector zoning in the centre and overgrowth zoning around the edges. Eudialyte 3-D unit cell measured with EBSD in solid white; (d) XPL thin-section image showing subhedral eudialyte with sector and overgrowth zoning. Eudialyte 3-D unit cell measured with EBSD in solid white; (e) EBSD phase map showing aegirine replacement of aenigmatite. Note the similar orientation of 3-D units cells of aenigmatite and aegirine; (f) EBSD phase map showing almost complete albitisation of orthoclase. Note the similar orientation of 3-D units cells of albite and orthoclase; (g) Combined band contrast and EBSD IPF map showing arfvedsonite growth within alkali feldspar grain. Note that arfvedsonite maintains its crystallographic orientation within the alkali feldspar grain. Arfvedsonite 3-D unit cells in white; (h) EBSD phase map showing albitisation of orthoclase, sodalite replacement of nepheline, and aegirine replacement of arfvedsonite. Note similar orientation of 3-D unit cells of nepheline and sodalite where the sodalite *a*-axis is parallel to one nepheline *a*-axis.

layer across the studied units (Fig. 10). Irregular grain boundaries and eudialyte overgrowth zoning peak in white layers and are nearly absent in black and red layers (Fig. 10). Mineral dissolution, albite replacement, impact nucleation, glomerocrysts, and mineral kinking/breaking peak in white layers, as well as at the transitions between black and red layers (Fig. 10). The glomerocryst trend varies slightly from the others in that it shows a gradual increase in numbers from the top of layer 0W through to layer +1B, whereas all the other microstructures above tend to decrease in layer +1B (Fig. 10).

DISCUSSION

Regardless of the mechanism by which a crystal mush forms, the initial interstitial liquid proportion within a crystal framework where crystals significantly impinge on one another is typically 50–70% (Irvine, 1980; Shirley, 1986; Philpotts *et al.*, 1998; Jerram *et al.*, 2003; Tegner *et al.*, 2009; Schmidt *et al.*, 2012). We record low interstitial mineral percentages, defined by the anhedral minerals occupying pore space between primocryst minerals, ranging from 10% in the black layers to 40% in the white layers (Figs 5a–c and 10). We recognise that the abundance of new interstitial

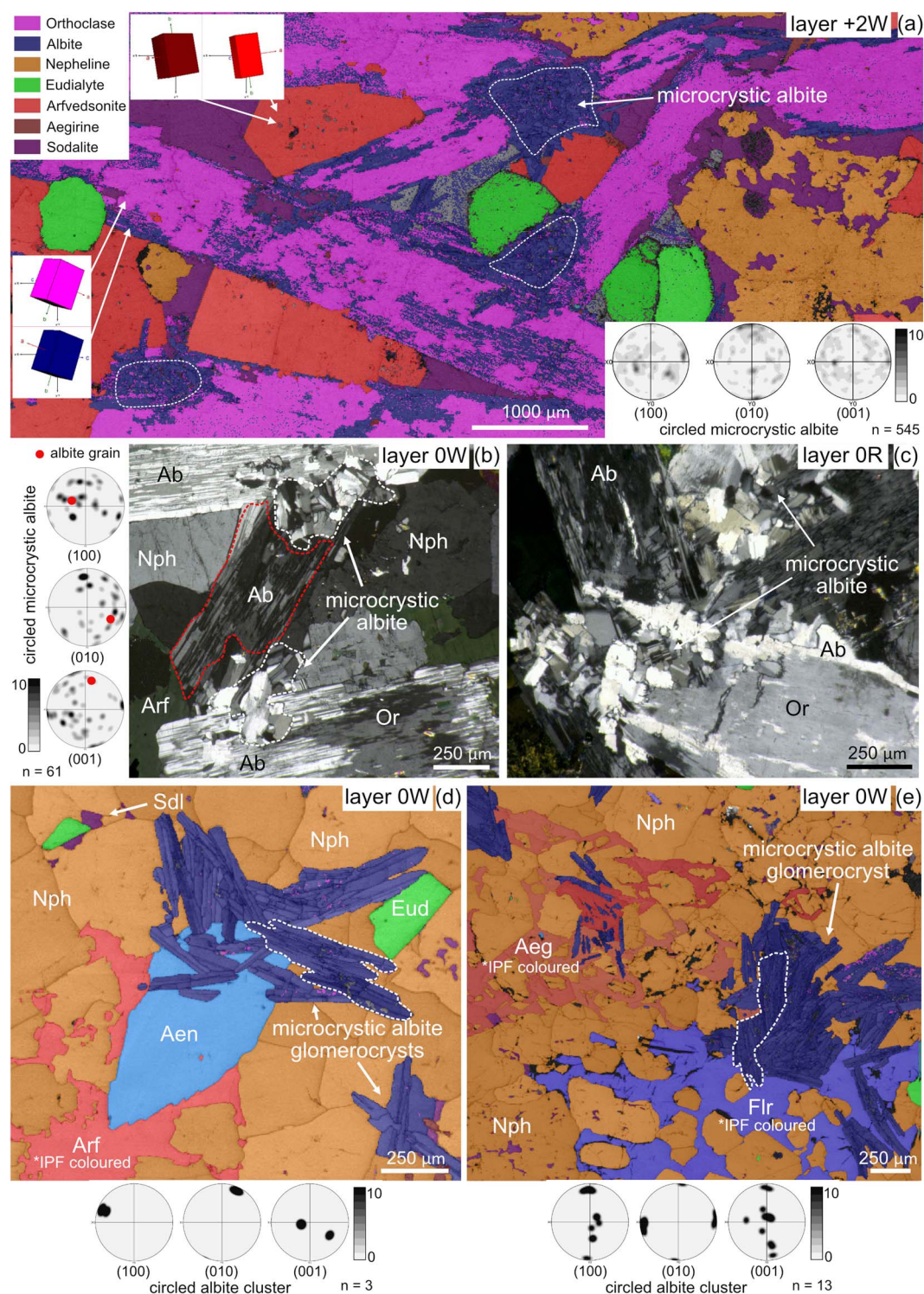


Fig. 9. Microcrystic grains within the kakortokites. Mineral abbreviations as in Figs 4 and 6. All pole figures are equal area, lower hemisphere, one averaged point per grain with n showing the number of grains. (a) EBSD phase map with pole figure of microcrystic albite grains. Note the similar orientations of 3-D unit cells of albite/orthoclase and arfvedsonite/aegirine; (b) XPL thin-section image showing clusters of microcrystic albite at contacts between alkali feldspar grains. Also displayed is the pole figure for the two clusters of microcrystic grains, with the orientation of the larger albite grain in red; (c) XPL thin-section image showing clusters of microcrystic albite at contacts between alkali feldspar grains; (d) EBSD phase map showing albite glomerocryst at contact between arfvedsonite oikocryst, aenigmatite grain, and nepheline groundmass. Arfvedsonite has been IPF-coloured showing maintained orientation of arfvedsonite across the oikocryst. A pole figure for a cluster of albite shows that albite crystals are in contact along their (010) faces; (e) EBSD phase map from layer 0W showing albite glomerocrysts within oikocrysts. Aegirine and fluorite have been IPF-coloured showing maintained orientation of the minerals across the oikocrysts. A pole figure for a cluster of albite shows albite crystals are in contact along their (010) faces.

minerals is not equivalent to the total interstitial material as this does not include interstitial overgrowths on existing phases. We also note that using interstitial mineral proportions in modally layered rocks to estimate residual liquid is complicated by the modally varying composition of different layers during crystallisation, possibly changing interstitial mineral phases and their proportions between layers. Therefore, our interstitial mineral percentages represent an approximate, minimum estimate for the amount of residual liquid within the mush (10–40%). Low quantities of interstitial material may be the result of post-accumulation primocryst growth through continued chemical transfer with the overlying bulk magma (e.g. Wager *et al.*, 1960; Wager, 1963; Campbell, 1978; Sparks *et al.*, 1985; Tait & Jaupart, 1992), or the physical loss of interstitial liquid potentially via compaction (e.g. Wager *et al.*, 1960; Sparks *et al.*, 1985; Tegner *et al.*, 2009; McKenzie, 2011; Schmidt *et al.*, 2012). Features such as magmatic foliations and crystal bending have been used to support hypotheses of liquid removal via compaction (e.g. Fiedrich *et al.*, 2017; Florez *et al.*, 2025), whereas fine-grained porphyritic textures and inverse zoning suggest other mechanisms, such as pressure changes during volcanic eruptions or thermal rejuvenation due to magma recharge, may result in liquid migration (e.g. Hartung *et al.*, 2017; Tavazzani *et al.*, 2020). Here, we first determine whether interstitial liquid migrated within the crystal pile and the role that compaction via viscous grain deformation may have played in crystal–melt separation, then discuss other possible mechanisms for the textures recorded in the kakortokites.

Were microstructures modified in the sub-solidus?

Before determining whether crystal–melt separation occurred and the role of compaction in that process, we need to establish whether any recrystallisation occurred that may have altered or overprinted pre-existing deformation microstructures. Euhedral alkali feldspar, eudialyte, and nepheline with arfvedsonite filling pore spaces in red and white layers is indicative of kinetic growth conditions (i.e. crystal growth in a liquid-rich environment) (Fig. 5b, c, e and f) (Holness, 2018). Additionally, tilting of alkali feldspar within white layers cannot be formed during solid-state deformation as it requires grain rotation (Fig. 7d). These textures are a strong indicator that these fabrics developed within the mush or at the mush–magma interface (Nicolas, 1992; Holness *et al.*, 2017). Conversely, curvilinear grain boundaries and 120° three-grain junctions in black layers (Figs 5a, b, d and 10) suggest that these horizons are approaching a modified microstructure (Fig. 1h and i). Such granular or equilibrated anisotropic microstructure can result from textural equilibration by grain boundary adjustment if the material is maintained at high temperatures or low degrees of undercooling (Piazolo *et al.*, 2004, 2005; Holness *et al.*, 2018). Critically, the presence of rounded arfvedsonite grains at the boundaries of liquid-filled pores suggests that grain boundaries became curvilinear while liquid was still present, which is inconsistent with sub-solidus recrystallisation (Fig. 6g and h). The complete lack of undulose extinction, mechanical twinning, and sub-grains in our samples also suggests little to no crystal deformation via dislocation creep occurred (Fig. 7c). Our samples do record occasional breaking and bending of alkali feldspar (Figs 7 and 10); however the orthoclase cores are undeformed (Fig. 7ciii) and the albite rims have internal misorientations reaching ~5° (Fig. 7civ), suggesting that the apparent changes in albite must have occurred independent from the orthoclase. We suggest that these features and the alkali feldspar lath shape of the albite–orthoclase domain are a result

of albite growth via a melt-mediated replacement reaction where an undeformed orthoclase is replaced, rather than late-stage deformation (Spruzeniec *et al.*, 2017). The observed curvilinear grain boundaries and 120° three-grain junctions most likely resulted from some degree of textural equilibration due to low degrees of undercooling or sustained high temperatures during crystallisation.

Evidence of liquid migration

Interstitial liquid that migrates to compositionally different horizons within a crystal mush will not initially be in chemical equilibrium with the primocryst minerals it contacts (e.g. Holness *et al.*, 2011; Humphreys, 2011). Therefore, we may expect the migration of interstitial liquid to be recorded through chemical disequilibrium features such as mineral replacement, resorption textures, zoning, and irregular grain boundaries (Solano *et al.*, 2014; Lissenberg & MacLeod, 2016; Zhang & Liu, 2023; Mangler *et al.*, 2024). In black layers, liquid pockets that are now represented by interstitial eudialyte, fluorite, and sodalite have highly attenuated apophyses and typically lack replacive textures (e.g. no mineral replacement or zoning) (Fig. 6g and h). In contrast to the equilibrium textures that characterise black layers, red and white layers have abundant (Fig. 10) late-stage interstitial minerals (albite, aegirine, and sodalite) that record mineral replacement (e.g. albitisation of orthoclase, sodalite replacement of nepheline, and aegirine replacement of arfvedsonite and aenigmatite, Figs 5g, 8f, h and 9a), overgrowth zoning on eudialyte (Fig. 8c and d), and irregular grain boundaries associated with oikocrysts (Fig. 6f). Below we will discuss each of these microstructures and their interpreted formation to further understand liquid migration through the crystal mush.

In our samples, albite replacement of orthoclase is epitaxial (see 3-D unit cells with similar orientations, Figs 8f and 9a) and typically associated with resorption textures of orthoclase, where surrounding arfvedsonite crystallises within the rims and central patches of the alkali feldspar (Figs 5i and 8g). Arfvedsonite included within alkali feldspar has the same crystallographic orientation as arfvedsonite outside alkali feldspar, suggesting that there was continuous growth of arfvedsonite from outside to within the alkali feldspar, coeval with albite crystallisation (Fig. 8g). As arfvedsonite is one of the main primocryst (black layers) and interstitial minerals (red and white layers), the coeval crystallisation of albite with arfvedsonite suggests that albitisation occurred early in the magmatic history of the kakortokites. The patchy nature of albitisation also suggests it is an early replacive feature, rather than a later stage exsolution feature (Figs 7a and 8f, h) (Schönwandt *et al.*, 2023). In addition to the albite replacement of orthoclase, nepheline is commonly replaced by sodalite (Figs 5g and 8f) and arfvedsonite/aenigmatite are replaced by aegirine (Fig. 8e and f). Albite, sodalite, and aegirine are all Na-rich phases; we suggest that these epitaxial mineral replacement features occurred coevally, and suggest that the liquid became increasingly Na-rich during the latter stages of primary magmatic crystallisation. Such a change in liquid composition is supported by: (1) the occurrence of albitisation, which is typically associated with the infiltration of Na-rich fluids into a magma (e.g. Lee & Parsons, 1997; Kaur *et al.*, 2012); and (2) the distinct appearance of eudialyte overgrowth zoning within white layers, and occasionally within red layers (Fig. 10). Specifically, we suggest that as the crystallisation of arfvedsonite appears to be concurrent with albitisation (Fig. 8g), it was a liquid enriched in Na that dissolved previously euhedral orthoclase, which was replaced with arfvedsonite and albite (Figs 8f, 9a and 11).

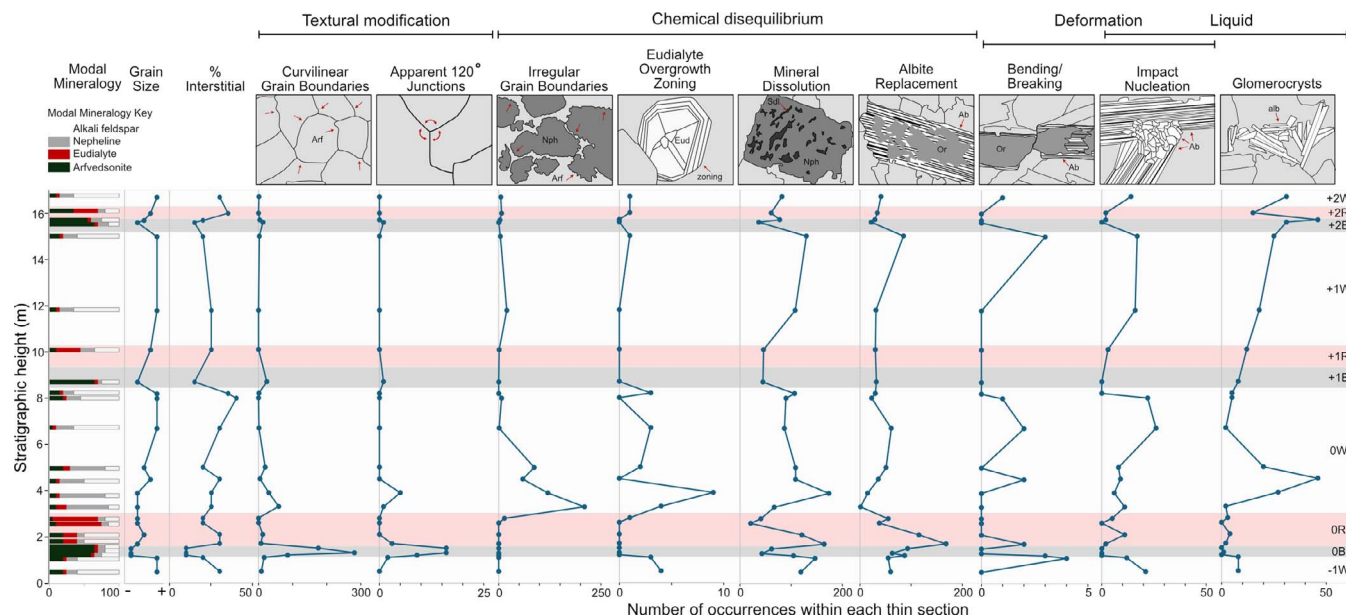


Fig. 10. Trends of mineral modes, grain size (of the main phase within each respective layer), proportion of interstitial minerals, and various microstructures through layers -1W to +2W of the kakortokites. Mineral abbreviations as in Fig. 4.

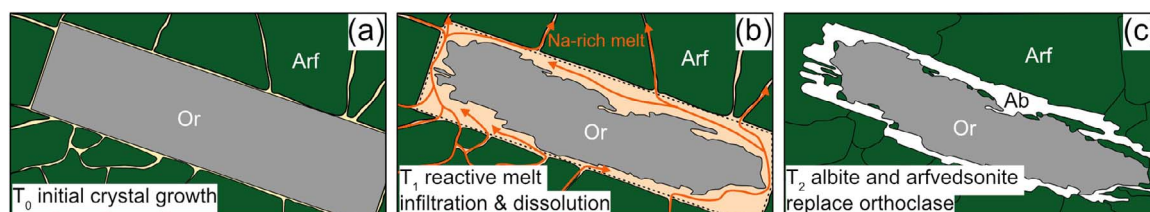


Fig. 11. Schematic of interface coupled replacement reactions involving local dissolution at reaction front along with immediate precipitation of arfvedsonite and albite.

Further evidence of chemical disequilibrium between the interstitial liquid and the primocrysts is the irregular grain boundaries around the nepheline chadacrysts within arfvedsonite and aegirine oikocrysts in white layers (Fig. 6f). Previous studies suggest oikocrysts may form *in situ* or by mechanical deposition as a primocryst phase (Barnes *et al.*, 2016; Latypov *et al.*, 2020). Primocryst oikocryst formation may be supported by a clear grain size distribution of the chadacrysts being smallest in the centre of the oikocryst and becoming increasingly large towards the edges of the oikocrysts; we observe a random grain size distribution of chadacrysts within our oikocrysts (Figs 5h and 6f), which is inconsistent with an *in situ* primocryst origin of the oikocrysts (Latypov *et al.*, 2020). Additionally, the nepheline chadacrysts within the oikocrysts have a random grain orientation (Fig. 6f); this is in contrast to the larger enclosing oikocrysts, which are commonly aligned along their long axes (Jones *et al.*, 2025). Irregular grain boundaries and differences in grain orientation between the oikocrysts and chadacrysts suggest that the oikocrysts crystallised relatively later than the nepheline, possibly filling liquid pockets within the unconsolidated mush (Fig. 12).

In summary, our observations of epitaxial Na-rich mineral replacement (see 3-D unit cells with similar orientations, Figs 8e, f, h and 9a), eudialyte overgrowth zoning (Fig. 8c and d), and irregular grain boundaries (Fig. 6d and f) support the interpretation of a vertically migrating interstitial, Na- and volatile-rich liquid through the crystal pile (Fig. 12). Whereas black layers only show minor albitisation as thin rims around the alkali feldspar,

albitisation is most pervasive within white layers and at black-layer transitions (Figs 8f and 9a–c). A similar trend is observed in the abundance of eudialyte overgrowth zoning and nepheline, arfvedsonite, and aenigmatite mineral replacement, which are highest in white layers (Fig. 10). We therefore suggest that the relative Na and volatile content of residual liquid increased in black layers and subsequently migrated up into overlying red and white layers (Fig. 12). Our interpretation of a vertically migrating interstitial liquid is consistent with: (1) the sub-vertical foliation defined by magnetite, orthogonal to igneous layering, measured by Jones *et al.* (2025); and (2) trace element geochemistry that shows eudialyte overgrowths locally follow differentiation paths that differ from the bulk melt (Borst *et al.*, 2018). Whereas eudialyte cores record a gradual upward decrease in Ca/(REE + Y), Fe/Mn, Ti, Nb, and Cl, eudialyte overgrowth rims record a compositional variability greater than the total stratigraphic changes recorded in the cores (Borst *et al.*, 2018). Borst *et al.* (2018) explain this phenomenon through the changes in co-crystallising mineral assemblages. However, co-crystallising minerals are unlikely to account for multiple abrupt changes in melt geochemistry (Tepper & Kuehner, 1999); we suggest the sharp, fine, concentric banding in the eudialyte overgrowth zoning is more consistent with a change in melt geochemistry due to interstitial liquid migration and homogenisation (Tepper & Kuehner, 1999; Streck, 2008). (Lindhuber *et al.*, 2015)(Lindhuber *et al.*, 2015).

The microstructural evidence discussed above clearly records an increase in disequilibrium textures from black layers into

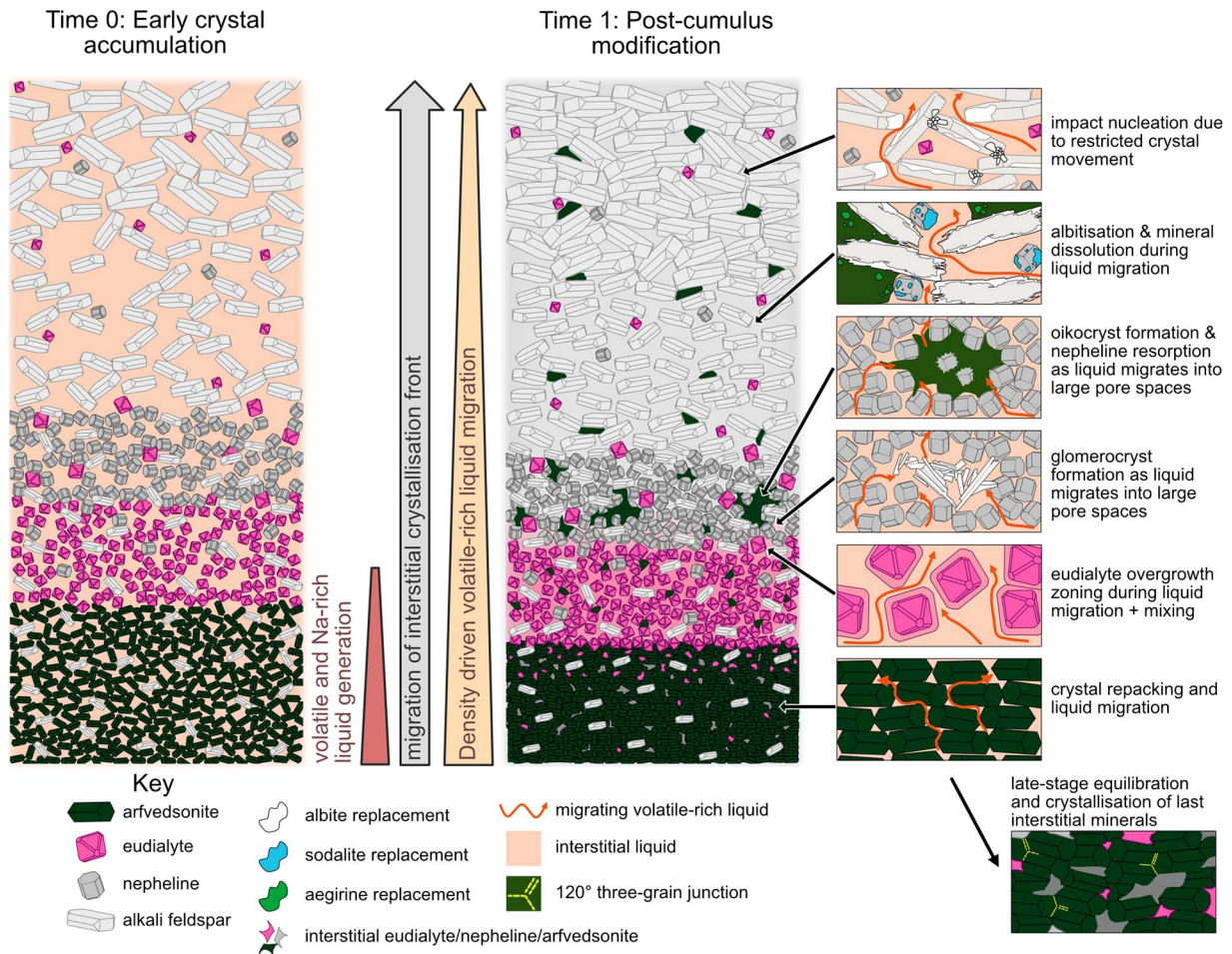


Fig. 12. Schematic representations of a three-layer unit during Time 0 (immediately following initial crystal accumulation), and Time 1 (following vertical migration of interstitial liquid). Zoom-ins highlight various microstructures identified within the kakortokites and their association with mechanical compaction and vertical liquid migration.

white layers, yet it is also possible that interstitial liquid also migrated between layered units. The presence of albite glomerocrysts within oikocrysts in layer 0W (Fig. 9d and e) suggests that these features formed at a similar time to albitisation and other Na-rich mineral replacements (e.g. sodalite and aegirine) late in the crystallisation sequence. We suggest that during vertical interstitial liquid migration, albite nucleated and grew within larger pore spaces of the crystal mush. To minimise interfacial energies (e.g. the interfacial energy between a crystal and liquid is higher than the energy between two crystals), elongate albite microcrysts amalgamated into glomerocrysts along their (010) faces (see pole figures, Fig. 9d and e) (Ikeda *et al.*, 2002; Holness & Vernon, 2015). Our interpretation of a late-stage albite nucleation event due to liquid migration is supported by alkali feldspar crystal size distribution data from three different outcrops of Unit 0 at Ilímaussaq, which recorded an upturned kink profile, a feature typically associated with late-stage nucleation (Hunt *et al.*, 2017). The steady increase in the number of glomerocrysts from the top of layer 0W through to layer +2R (Fig. 10) suggests that interstitial liquid likely migrated vertically through three-layer units, travelling from Unit 0, through Unit +1, and into Unit +2. This vertical liquid migration through units is supported by the findings of Jones *et al.* (2025), who identify independent subvertical mineral lineations that are interpreted to represent interstitial liquid remobilisation through gently inclined modal igneous layers.

The role of compaction via viscous grain deformation in crystal–melt separation

Compaction via viscous grain deformation is commonly cited as the principal mechanism that drives the separation of crystals and melt within a crystal mush (e.g. Tegner *et al.*, 2009; McKenzie, 2011; Latypov *et al.*, 2024). While we observe only rare bending and breaking of alkali feldspar in white layers (Fig. 7), no evidence of undulose extinction or sub-grains is identified in any samples (Fig. 7ciii and civ); the absence of these microstructures is inconsistent with compaction occurring via dislocation creep. Alternatively, compaction can occur via diffusion and/or dissolution–precipitation (e.g. Holness *et al.*, 2017). During dissolution–precipitation, grains with an ‘unfavourable’ orientation (i.e. their long axis is parallel to the direction of maximum stress) are dissolved and reprecipitated in favourable orientations resulting in asymmetric chemical changes and a general shape preferred orientation of elongated grains perpendicular to the main stress axis (Fig. 1g) (Meurer & Boudreau, 1998b; Boorman *et al.*, 2004; Holness *et al.*, 2017, 2018). Mineral zoning is identified in both arfvedsonite and eudialyte within the samples; however the zoning appears to be nearly uniform in width around the grain edges and occurs in grains with varying orientations (note the horizontal of all thin sections is parallel to igneous layering, Fig. 8a, c and d) and therefore is unlikely to represent crystal growth in low-stress orientations. The exception to this is the rare curvilinear zoning in arfvedsonite that is confined to certain grain edges; however

these form on a variety of grain boundary orientations, including the upper grain boundary (Fig. 8b), which we would expect to be the main stress orientation during compaction (Fig. 1g). We suggest this zoning is a result of grain boundary migration during textural equilibration, rather than anisotropic overgrowth during compaction. The zoning morphologies, as well as the lack of observed grain truncation and sutured contacts, suggests that significant compaction via diffusion creep and/or dissolution–precipitation did not occur.

The lack of evidence for compaction via viscous grain deformation by either dislocation, diffusion, or dissolution–precipitation creep in our samples is consistent with earlier studies that suggest compaction via viscous grain deformation is likely not a significant process in intrusions with evolved compositions (Holness *et al.*, 2017; Holness, 2018; Vukmanovic *et al.*, 2019). Compaction via viscous grain deformation is more likely to operate in large, deep intrusions where the mush comprises high proportions of dense primocryst minerals such as oxides, which would provide a sufficient gravitational load for compaction with sufficiently high stresses to occur (Holness *et al.*, 2017).

Crystal–melt separation in the kakortokites: mechanisms, consequences, and implications

Crystal repacking (i.e. mechanical compaction) is consistent with observations of obliquity between the silicate mineral foliation and the attitude of modal igneous layering measured by Jones *et al.* (2025), tilting and draping of alkali feldspar around other primocryst minerals, such as nepheline (Figs 5c and 7b, d), and the breaking/bending of alkali feldspar where crystals are more densely packed (Fig. 7) (Hunter, 1996; Philpotts & Philpotts, 2005). The stresses required to break alkali feldspar in white layers were likely small, as the feldspar crystal structure may have been weakened by dissolution and preferential pressure solution at grain contacts (e.g. Paterson, 1973; Imon *et al.*, 2002). Crystal repacking is also consistent with the observation of microcrystic albite clusters at intersecting alkali feldspar grains, which we term ‘impact nucleation’ (Fig. 9a–c). During crystal rearrangement, where crystals are densely packed, adjacent grains may create a region of relatively higher stress (see force chains of Bergantz *et al.* (2017)). These sites likely provided an advantageous surface for late-stage albite nucleation, as heterogeneous nucleation preferentially occurs in areas with higher stress (e.g. Zeng & Xu, 2015; Holness *et al.*, 2023). Therefore, the distribution of mineral kinking, breaking, and albite nucleation microstructures in our samples, which are concentrated within white layers (Fig. 9), is likely a record of the ability of the crystal pile to repack during mechanical compaction (Fig. 12).

In addition to mechanical compaction, magma recharge/flow, gas filter-pressing, and/or convection of interstitial liquid may contribute to crystal–melt separation (e.g. Anderson *et al.*, 1984; Sparks *et al.*, 1985; Tait & Jaupart, 1992; Boudreau, 2016; Lissenberg *et al.*, 2019; Vukmanovic *et al.*, 2019). A lack of magma injection fabrics (Jones *et al.*, 2025) and geochemical work across the kakortokite sequence (units –11 to +16) that records a continuous evolution of a single apaitic bulk melt (Borst *et al.*, 2018), together suggest that magma recharge/flow is likely not responsible for crystal–melt separation in the kakortokites (e.g. Petford *et al.*, 2000; Davis *et al.*, 2007; Holness *et al.*, 2017; Bachmann & Huber, 2019). Gas filter-pressing may have occurred within the kakortokites, as Ilímaussaq crystallised at 3–4 km depth and had an H₂O content of 4 wt % (Larsen & Sørensen, 1987; Markl *et al.*, 2001; Garde *et al.*, 2002; Krumrei *et al.*, 2006; Upton, 2013), which is within the range of gas filter-pressing being an effective

liquid migration mechanism (Sisson & Bacon, 1999). However, in volatile-rich systems such as the peralkaline melts of the kakortokites (Larsen & Sørensen, 1987), gas filter-pressing is likely to be limited as pressure from exsolved volatiles may prevent liquid transfer within the mush or create channels that release the pressure gradient required for filter-pressing (Oppenheimer *et al.*, 2015; Parmigiani *et al.*, 2016; Bachmann & Huber, 2019). Alternatively, compositional or thermal convection of interstitial liquid may have occurred, which relies on the density of interstitial liquid decreasing with continued fractionation, such that the density profile of the interstitial liquid decreases upwards and is therefore unstable (Sparks *et al.*, 1985; Tait & Jaupart, 1992). While the density of residual liquid within mafic systems is well understood, the changes in density of a volatile-rich peralkaline liquid have not been thoroughly studied. It is possible that in black layers where arfvedsonite (the densest of the primocryst minerals within the three-layer unit, Bons *et al.* (2015)) is volumetrically dominant, the residual liquid was significantly less dense and buoyantly rose into overlying white layers. In contrast, alkali feldspar growth in white layers may have increased the density of the residual liquid in these horizons, leading to convective exchange of interstitial liquid between black and white layers. Further work into density changes of evolving peralkaline melts would help elucidate the role of convection in these mush systems.

An important consideration for crystal–melt separation mechanisms is the phases present within a mush (i.e. solids, liquids, fluids, and gases) (e.g. Parmigiani *et al.*, 2011, 2016; Huber & Parmigiani, 2018). As discussed above, the exsolution of a magmatic volatile phase may hinder liquid migration due to changes in pressure gradients or the formation of channels within the crystal framework (e.g. Bachmann & Huber, 2019). Microcrystic albite glomerocrysts identified within our samples (Fig. 9d and e) may be a record of volatile exsolution due to second boiling (i.e. crystallisation-induced exsolution, Candela (1994)) within the mush, as feldspar microlites typically crystallise due to a loss of volatiles (H₂O) (Hammer *et al.*, 1999; Cashman & Blundy, 2000; Hammer, 2008; Shea & Hammer, 2013; Cáceres *et al.*, 2022). This is consistent with fluid inclusion data from naujaite roof rocks (Fig. 2a) and geochemical data from ‘spheroidal structures’ within the lujavrites (Fig. 2a), which suggest that CH₄-rich fluids, highly saline, H₂O-rich fluids, and immiscible H₂O-rich liquids exsolved from the peralkaline melt at Ilímaussaq (Konnerup-Madsen *et al.*, 1979; Konnerup-Madsen & Rose-Hansen, 1982; Sørensen *et al.*, 2003). Vertical migration of an Na- and volatile-rich phase (Fig. 12) is supported by our observations of albitisation (Figs 5i and 8f, h), sodalite replacement of nepheline (Fig. 8h), and aegirine replacement of arfvedsonite/aenigmatite (Fig. 8e and h), which increase vertically through a three-layer unit (Fig. 10). In the absence of fluid and melt inclusion data from these replacive mineral phases, it is not possible to discern whether the migrating volatile-rich phase was a silicate liquid, aqueous fluid, or perhaps a combination of the two. However, a volatile-rich phase, whether a silicate liquid or aqueous fluid, would likely have a lower viscosity and density than the residual liquid, and thus vertically migrate through the mush (Larsen & Sørensen, 1987). Therefore, the kakortokite crystal mush likely had co-existing volatile-rich silicate liquid and aqueous fluid phases, which vertically migrated through buoyancy, capillary stress, and viscosity (e.g. Parmigiani *et al.*, 2011, 2016; Boudreau, 2016; Huber & Parmigiani, 2018).

In summary, mechanical compaction and volatile-rich phase migration are significant mechanisms within the layered

nepheline syenites at Ilímaussaq. The distribution of different microstructures within our samples demonstrates that the efficiency of these mechanisms is impacted by crystal size, shape, and distribution (i.e. mush permeability) vertically through a crystal pile. The layers likely initially formed via gravitational settling and the development of crystal mats as suggested by eudialyte geochemical trends and consistent mineral foliations identified in previous studies (e.g. Lindhuber *et al.*, 2015; Borst *et al.*, 2018; Jones *et al.*, 2025). As the crystal mats further developed, mush compartments formed with basal arfvedsonite-rich and upper alkali feldspar-rich layers (Borst *et al.*, 2018). Within these mush compartments, eudialyte-rich red layers continued to crystallise as the residual liquid fractionated. Critically, the stability of eudialyte, the main REE ore mineral, is lessened in the presence of volatiles (Nikolenko *et al.*, 2024). Thus, the vertical migration of volatile-rich phases during compaction, as identified in this study, may be significant for the development of eudialyte REE-rich layers. By using microstructures such as microcrystic grains, mineral kinking, mineral replacement and mineral zoning to track compaction and volatile phase migration, and features such as grain size, boundaries, and junctions to track mush permeability, we can better target horizons of REE concentration within alkaline-layered intrusions.

CONCLUSIONS

Combined petrography and microstructural analysis, including quantitative crystallographic orientation analysis (EBSD), provides detailed records of mechanical compaction and vertical interstitial liquid and volatile migration within a crystal mush. Whereas curvilinear grain boundaries and apparent 120° three-grain junctions suggest black layers were approaching textural equilibrium, extensive albitisation, mineral dissolution and replacement, and eudialyte overgrowth zoning across red and white layers record vertically increasing disequilibrium within a three-layer unit. We suggest the increase in disequilibrium between crystals and liquid within a three-layer unit is due to vertical migration of a volatile-rich liquid from black layers into white layers. The distribution of microcrystic albite glomerocrysts suggests the volatile-rich liquid also migrated vertically between three-layer units, demonstrating liquid communication and connectivity through the crystal pile. We record no evidence of viscous grain deformation (e.g. undulose extinction, mechanical twinning, sub-grains), and only rare bending or breaking of alkali feldspar, suggesting that compaction via viscous grain deformation was not the primary mechanism for vertical volatile-rich liquid migration. Tiling and draping of anisotropic minerals such as alkali feldspar, as well as clusters of microcrystic albite at mineral intersections, suggest crystal repacking (i.e. mechanical compaction) of the crystal pile occurred. Our findings support the growing body of microstructural evidence that compaction via viscous grain deformation is not a significant mechanism in crystal–melt separation within intrusions with chemically evolved compositions. Our observations suggest that late-stage interstitial volatile-rich liquid migration occurs vertically through igneous layers, potentially modifying primary layering features. The ability for volatile-rich liquid to migrate through the crystal pile has implications for the stability of eudialyte, the main REE ore mineral, and therefore microstructures provide a means for tracking likely horizons of REE concentration within alkaline-layered intrusions.

SUPPLEMENTARY DATA

Supplementary data are available at *Journal of Petrology* online.

ACKNOWLEDGEMENTS

Field context and samples were collected for this study during a field expedition to Ilímaussaq in 2022. We thank Tesni Morgan, Aithne Lawrence, Nina Brendling, Yasamin Bayley, and Brogan Smith for their support during the field expedition. The expedition was funded by the Gino Watkins Memorial Fund, the Arctic Club, the Society of Economic Geologists, the Cambridge Arctic Shelf Programme, the Volcanic and Magmatic Studies Group, the Hazel-Prichard Student Bursary, the Geological Society of London, and the Edinburgh Geological Society. We also thank A. Boudreau and C. Huber for detailed and constructive reviews and V. Troll for editorial handling.

FUNDING

This work was supported by the Natural Environment Research Council via an IAPETUS2 PhD studentship held by E.J. (grant number NE/S007431/1). W.H. is funded by a UKRI Future Leaders Fellowship (grant number MR/S033505/1).

DATA AVAILABILITY

Data are available in a repository and can be accessed at: [<https://doi.pangaea.de/10.1594/PANGAEA.982612>].

REFERENCES

- Andersen, S., Bohse, H. & Steenfelt, A. (1981). A geological section through the southern part of the Ilímaussaq intrusion. *Rapport Grønlands Geologiske Undersøgelse* **103**, 39–42. <https://doi.org/10.34194/rapggv.v103.7729>.
- Anderson, A. T., Swihart, G. H., Artioli, G. & Geiger, C. A. (1984). Segregation vesicles, gas filter-pressing, and igneous differentiation. *Journal of Geology* **92**, 55–72. <https://doi.org/10.1086/628834>.
- Asimus, J. L., Daczko, N. R., Gazi, J. A., Ezad, I. S., Belousov, I., Rodemann, T., Halpin, J. A. & Piazzolo, S. (2024). Experimental replacement of zircon by melt-mediated coupled dissolution-precipitation causes dispersion in U–Pb ages. *Journal of Metamorphic Geology*. <https://doi.org/10.1111/jmg.12795>.
- Bachmann, O. & Bergantz, G. W. (2004). On the origin of crystal-poor rhyolites: extracted from batholithic crystal mushes. *Journal of Petrology* **45**(8), 1565–1582. <https://doi.org/10.1093/petrology/egh019>.
- Bachmann, O. & Huber, C. (2019). The inner workings of crustal distillation columns; the physical mechanisms and rates controlling phase separation in silicic magma reservoirs. *Journal of Petrology* **60**(1), 3–18. <https://doi.org/10.1093/petrology/egy103>.
- Barnes, S. J., Mole, D. R., Le Vaillant, M., Campbell, M. J., Verrall, M. R., Roberts, M. P. & Evans, N. J. (2016). Poikilitic textures, heteroaccumulates and zoned orthopyroxenes in the Ntaka ultramafic complex, Tanzania: implications for crystallization mechanisms of oikocrysts. *Journal of Petrology* **57**(6), 1171–1198. <https://doi.org/10.1093/petrology/egw036>.
- Bartley, J. M., Glazner, A. F. & Coleman, D. S. (2018). Dike intrusion and deformation during growth of the Half Dome pluton, Yosemite National Park, California. *Geosphere* **14**(3), 1283–1297. <https://doi.org/10.1130/GES01458.1>.

- Beard, C. D., Goodenough, K. M., Borst, A. M., Wall, F., Siegfried, P. R., Deady, E. A., Pohl, C., Hutchison, W., Finch, A. A., Walter, B. F., Elliott, H. A. L. & Brauch, K. (2023). Alkaline-silicate REE-HFSE systems. *Economic Geology* **118**(1), 177–208. <https://doi.org/10.5382/econgeo.4956>.
- Bennett, E. N., Lissenberg, C. J. & Cashman, K. V. (2019). The significance of plagioclase textures in mid-ocean ridge basalt (Gakkel Ridge, Arctic Ocean). *Contributions to Mineralogy and Petrology* **174**(6), 49. <https://doi.org/10.1007/s00410-019-1587-1>.
- Bergantz, G. W., Schleicher, J. M. & Burgisser, A. (2017). On the kinematics and dynamics of crystal-rich systems. *Journal of Geophysical Research: Solid Earth* **122**(8), 6131–6159. <https://doi.org/10.1002/2017JB014218>.
- Bertolett, E. M., Prior, D. J., Gravley, D. M., Hampton, S. J. & Kennedy, B. M. (2019). Compacted cumulates revealed by electron backscatter diffraction analysis of plutonic lithics. *Geology* **47**(5), 445–448. <https://doi.org/10.1130/G45616.1>.
- Bohse, H., Brooks, C. K. & Kunzendorf, H. (1971). Field observations on the kakortokites of the Ilímaussaq intrusion, South Greenland, including mapping and analyses by portable X-ray fluorescence equipment for zirconium and niobium. *Rapport Grønlands Geologiske Undersøgelse* **38**, 1–43. <https://doi.org/10.34194/rapggv.v38.7278>.
- Bons, P. D., Jessell, M. W., Evans, L., Barr, T. & Stüwe, K. (2001). Modeling of anisotropic grain growth in minerals. *Memoir of the Geological Society of America* **193**, 39–49. <https://doi.org/10.1130/0-8137-1193-2.39>.
- Bons, P. D., Baur, A., Elburg, M. A., Lindhuber, M. J., Marks, M. A. W., Soesoo, A., Van Milligen, B. P. & Walte, N. P. (2015). Layered intrusions and traffic jams. *Geology* **43**(1), 71–74. <https://doi.org/10.1130/G36276.1>.
- Boorman, S., Boudreau, A. E. & Kruger, F. J. (2004). The lower zone-critical zone transition of the Bushveld complex: a quantitative textural study. *Journal of Petrology* **45**(6), 1209–1235. <https://doi.org/10.1093/petrology/egh011>.
- Borst, A. M., Friis, H., Nielsen, T. F. D. & Waight, T. E. (2018). Bulk and mush melt evolution in agpaite intrusions: insights from compositional zoning in eudialyte, Ilímaussaq complex, South Greenland. *Journal of Petrology* **59**(4), 589–612. <https://doi.org/10.1093/petrology/egy038>.
- Borst, A. M., Waight, T. E., Finch, A. A., Storey, M. & Roux, P. J. L. (2019). Dating agpaite rocks: a multi-system (U/Pb, Sm/Nd, Rb/Sr and ⁴⁰Ar/³⁹Ar) isotopic study of layered nepheline syenites from the Ilímaussaq complex, Greenland. *Lithos* **324–325**, 74–88. <https://doi.org/10.1016/j.lithos.2018.10.037>.
- Boudreau, A. E. (2016). Bubble migration in a compacting crystalline liquid mush. *Contributions to Mineralogy and Petrology* **171**(4). <https://doi.org/10.1007/s00410-016-1237-9>.
- Boudreau, A. E. & McCallum, I. S. (1992). Infiltration metasomatism in layered intrusions - an example from the Stillwater complex, Montana. *Journal of Volcanology and Geothermal Research* **52**, 171–183. [https://doi.org/10.1016/0377-0273\(92\)90139-5](https://doi.org/10.1016/0377-0273(92)90139-5).
- Boudreau, A. E. & Meurer, W. P. (1999). Chromatographic separation of the platinum-group elements, gold, base metals and sulfur during degassing of a compacting and solidifying igneous crystal pile. *Contributions to Mineralogy and Petrology* **134**, 174–185. <https://doi.org/10.1007/s004100050477>.
- Boulanger, M. & France, L. (2023). Cumulate formation and melt extraction from mush-dominated magma reservoirs: the melt flush process exemplified at mid-ocean ridges. *Journal of Petrology* **64**(2). <https://doi.org/10.1093/petrology/egad005>.
- Cáceres, F., Scheu, B., Colombier, M., Hess, K. U., Feisel, Y., Ruthensteiner, B. & Dingwell, D. B. (2022). The roles of microlites and phenocrysts during degassing of silicic magma. *Earth and Planetary Science Letters* **577**, 117264. <https://doi.org/10.1016/j.epsl.2021.117264>.
- Campbell, I. H. (1978). Some problems with the cumulus theory. *Lithos* **11**, 311–323. [https://doi.org/10.1016/0024-4937\(78\)90038-5](https://doi.org/10.1016/0024-4937(78)90038-5).
- Candela, P. A. (1994). Combined chemical and physical model for plutonic devolatilization: a non-Rayleigh fractionation algorithm. *Geochimica et Cosmochimica Acta* **58**(10), 2157–2167. [https://doi.org/10.1016/0016-7037\(94\)90002-7](https://doi.org/10.1016/0016-7037(94)90002-7).
- Cashman, K. & Blundy, J. (2000). Degassing and crystallization of ascending andesite and dacite. *Philosophical Transactions of the Royal Society of London* **358**(1770), 1487–1513. <https://doi.org/10.1098/rsta.2000.0600>.
- Cashman, K. & Blundy, J. (2013). Petrological cannibalism: the chemical and textural consequences of incremental magma body growth. *Contributions to Mineralogy and Petrology* **166**(3), 703–729. <https://doi.org/10.1007/s00410-013-0895-0>.
- Chadam, J., Hoff, D., Merino, E., Ortoleva, P. & Sen, A. A. (1986). Reactive infiltration instabilities. *IMA Journal of Applied Mathematics* **36**, 207–221. <https://doi.org/10.1093/imamat/36.3.207>.
- Connolly, J. A. D. & Schmidt, M. W. (2022). Viscosity of crystal-mushes and implications for compaction-driven fluid flow. *Journal of Geophysical Research: Solid Earth* **127**(9). <https://doi.org/10.1029/2022JB024743>.
- Cooper, R. F. & Kohlstedt, D. L. (1984). Solution-precipitation enhanced diffusional creep of partially molten olivine-basalt aggregates during hot-pressing. *Tectonophysics* **107**, 207–233. [https://doi.org/10.1016/0040-1951\(84\)90252-X](https://doi.org/10.1016/0040-1951(84)90252-X).
- Couch, S., Sparks, R. S. J. & Carroll, M. R. (2001). Mineral disequilibrium in lavas explained by convective self-mixing in open magma chambers. *Nature* **411**, 1037–1039. <https://doi.org/10.1038/35082540>.
- Cross, A. J. & Skemer, P. (2019). Rates of dynamic recrystallization in geologic materials. *Journal of Geophysical Research: Solid Earth* **124**(2), 1324–1342. <https://doi.org/10.1029/2018JB016201>.
- Davis, M., Koenders, M. A. & Petford, N. (2007). Vibro-agitation of chambered magma. *Journal of Volcanology and Geothermal Research* **167**(1–4), 24–36. <https://doi.org/10.1016/j.jvolgeores.2007.07.012>.
- Donev, A., Cisse, I., Sachs, D., Variano, E. A., Stillinger, F. H., Connelly, R., Torquato, S. & Chaikin, P. M. (2004). Improving the density of jammed disordered packings using ellipsoids. *High Temperatures - High Pressures* **303**, 990–993. <https://doi.org/10.1126/science.1093010>.
- Drury, M. R. & Urai, J. L. (1990). Deformation-related recrystallization processes. *Tectonophysics* **172**, 235–253. [https://doi.org/10.1016/0040-1951\(90\)90033-5](https://doi.org/10.1016/0040-1951(90)90033-5).
- Ferguson, J. (1964). Geology of the Ilímaussaq alkaline intrusion, South Greenland. *Grønlands Geologiske Undersøgelse* **39**, 1–82. <https://doi.org/10.34194/bullggv.v39.6573>.
- Fiedrich, A. M., Bachmann, O., Ulmer, P., Deering, C. D., Kunze, K. & Leuthold, J. (2017). Mineralogical, geochemical, and textural indicators of crystal accumulation in the Adamello batholith (northern Italy). *American Mineralogist* **102**(12), 2467–2483. <https://doi.org/10.2138/am-2017-6026>.
- Florez, D., Huber, C., Hoyos, S., Pec, M., Parmentier, E. M., Connolly, J. A. D. & Hirth, G. (2024). Repacking in compacting mushes at intermediate melt fractions: constraints from numerical modeling and phase separation experiments on granular media. *Journal of Geophysical Research: Solid Earth* **129**(7). <https://doi.org/10.1029/2024jb029077>.
- Florez, D., Huber, C., Bachmann, O., Sigworth, A., Claiborne, L. & Miller, C. (2025). Repacking-driven compaction in the Spirit

- Mountain batholith, southern Nevada. *Journal of Petrology* **66**(2). <https://doi.org/10.1093/petrology/egaf003>.
- Garde, A. A., Hamilton, M. A., Chadwick, B., Grocott, J. & McCaffrey, K. J. W. (2002). The Ketilidian orogen of South Greenland: geochronology, tectonics, magmatism, and fore-arc accretion during Palaeoproterozoic oblique convergence. *Canadian Journal of Earth Sciences* **39**(5), 765–793. <https://doi.org/10.1139/e02-026>.
- Giehl, C., Marks, M. & Nowak, M. (2013). Phase relations and liquid lines of descent of an iron-rich peralkaline phonolitic melt: an experimental study. *Contributions to Mineralogy and Petrology* **165**(2), 283–304. <https://doi.org/10.1007/s00410-012-0809-6>.
- Giehl, C., Marks, M. A. W. & Nowak, M. (2014). An experimental study on the influence of fluorine and chlorine on phase relations in peralkaline phonolitic melts. *Contributions to Mineralogy and Petrology* **167**(3), 1–21. <https://doi.org/10.1007/s00410-014-0977-7>.
- Glazner, A. F. & Boudreau, A. (2011). Metamorphism of through about igneous rock textures. *International Geology Review* **53**(3–4), 327–329. <https://doi.org/10.1080/00206814.2010.496165>.
- Gleeson, M. L. M., Lissenberg, C. J. & Antoshechkina, P. M. (2023). Porosity evolution of mafic crystal mush during reactive flow. *Nature Communications* **14**(1). <https://doi.org/10.1038/s41467-023-38136-x>.
- Gray, N. H., Philpotts, A. R. & Dickson, L. D. (2003). Quantitative measures of textural anisotropy resulting from magmatic compaction illustrated by a sample from the Palisades sill, New Jersey. *Journal of Volcanology and Geothermal Research* **121**, 293–312. [https://doi.org/10.1016/S0377-0273\(02\)00463-8](https://doi.org/10.1016/S0377-0273(02)00463-8).
- Guillope, M. & Poirier, J. P. (1979). Dynamic recrystallization during creep of single-crystalline halite: an experimental study. *Journal of Geophysical Research* **84**(B10), 5557–5567. <https://doi.org/10.1029/JB084iB10p05557>.
- Hammer, J. E. (2008). Experimental studies of the kinetics and energetics of magma crystallization. *Reviews in Mineralogy and Geochemistry* **69**, 9–59. <https://doi.org/10.2138/rmg.2008.69.2>.
- Hammer, J. E., Cashman, K. V., Hoblitt, R. P. & Newman, S. (1999). Degassing and microlite crystallization during pre-climactic events of the 1991 eruption of Mt. Pinatubo, Philippines. *Bulletin of Volcanology* **60**, 355–380. <https://doi.org/10.1007/s004450050238>.
- Hammer, J. E., Sharp, T. G. & Wessel, P. (2010). Heterogeneous nucleation and epitaxial crystal growth of magmatic minerals. *Geology* **38**(4), 367–370. <https://doi.org/10.1130/G30601.1>.
- Hartung, E., Caricchi, L., Floess, D., Wallis, S., Harayama, S., Kouzmanov, K. & Chiaradia, M. (2017). Evidence for residual melt extraction in the Takidani pluton, Central Japan. *Journal of Petrology* **58**(4), 763–788. <https://doi.org/10.1093/petrology/egx033>.
- Higgins, M. D. (2011). Textural coarsening in igneous rocks. *International Geology Review* **53**(3–4), 354–376. <https://doi.org/10.1080/00206814.2010.496177>.
- Higgins, M. D. (2015). Quantitative textural analysis of rocks in layered mafic intrusions. In: Charlier et al. (eds) *Springer Geology*. Dordrecht: Springer, pp.153–181.
- Hirth, G. & Kohlstedt, D. L. (1995). Experimental constraints on the dynamics of the partially molten upper mantle: deformation in the diffusion creep regime. *Journal of Geophysical Research* **100**(B2), 1981–2001. <https://doi.org/10.1029/94JB02128>.
- Hirth, G. & Tullis, J. (1992). Dislocation creep regimes in quartz aggregates. *Journal of Structural Geology* **14**(2), 145–159. [https://doi.org/10.1016/0191-8141\(92\)90053-Y](https://doi.org/10.1016/0191-8141(92)90053-Y).
- Holness, M. B. (2005). Spatial constraints on magma chamber replenishment events from textural observations of cumulates: the Rum layered intrusion, Scotland. *Journal of Petrology* **46**(8), 1585–1601. <https://doi.org/10.1093/petrology/egi027>.
- Holness, M. B. (2007). Textural immaturity of cumulates as an indicator of magma chamber processes: infiltration and crystal accumulation in the Rum eastern layered intrusion. *Journal of the Geological Society* **164**, 529–539. <https://doi.org/10.1144/0016-76492006-021>.
- Holness, M. B. (2018). Melt segregation from silicic crystal mushes: a critical appraisal of possible mechanisms and their microstructural record. *Contributions to Mineralogy and Petrology* **173**(6), 48. <https://doi.org/10.1007/s00410-018-1465-2>.
- Holness, M. B. & Fowler, A. C. (2022). The formation of three-grain junctions during solidification. Part I: observations. *Contributions to Mineralogy and Petrology* **177**(5). <https://doi.org/10.1007/s00410-022-01917-6>.
- Holness, M. B. & Siklos, S. T. C. (2000). The rates and extent of textural equilibration in high-temperature fluid-bearing systems. *Chemical Geology* **162**, 137–153. [https://doi.org/10.1016/S0009-2541\(99\)00124-2](https://doi.org/10.1016/S0009-2541(99)00124-2).
- Holness, M. B. & Vernon, R. H. (2015). The Influence of interfacial energies on igneous microstructures. In: Charlier et al. (eds) *Springer Geology*. Dordrecht: Springer, pp.183–228.
- Holness, M. B., Cheadle, M. J. & McKenzie, D. (2005). On the use of changes in dihedral angle to decode late-stage textural evolution in cumulates. *Journal of Petrology* **46**(8), 1565–1583. <https://doi.org/10.1093/petrology/egi026>.
- Holness, M. B., Nielsen, T. F. D. & Tegner, C. (2007). Textural maturity of cumulates: a record of chamber filling, liquidus assemblage, cooling rate and large-scale convection in mafic layered intrusions. *Journal of Petrology* **48**(1), 141–157. <https://doi.org/10.1093/petrology/egl057>.
- Holness, M. B., Stripp, G., Humphreys, M. C. S., Veksler, I. V., Nielsen, T. F. D. & Tegner, C. (2011). Silicate liquid immiscibility within the crystal mush: late-stage magmatic microstructures in the Skaergaard intrusion, East Greenland. *Journal of Petrology* **52**(1), 175–222. <https://doi.org/10.1093/petrology/egq077>.
- Holness, M. B., Vukmanovic, Z. & Mariani, E. (2017). Assessing the role of compaction in the formation of adcumulates: a microstructural perspective. *Journal of Petrology* **58**(4), 643–673. <https://doi.org/10.1093/petrology/egx037>.
- Holness, M. B., Clemens, J. D. & Vernon, R. H. (2018). How deceptive are microstructures in granitic rocks? Answers from integrated physical theory, phase equilibrium, and direct observations. *Contributions to Mineralogy and Petrology* **173**(8), 62–18. <https://doi.org/10.1007/s00410-018-1488-8>.
- Holness, M. B., Stock, M. J. & Geist, D. (2019). Magma chambers versus mush zones: constraining the architecture of sub-volcanic plumbing systems from microstructural analysis of crystalline enclaves. *Philosophical Transactions of the Royal Society A: Mathematical, Physical and Engineering Sciences* **377**(2139), 20180006. <https://doi.org/10.1098/rsta.2018.0006>.
- Holness, M. B., Vukmanovic, Z. & O'Driscoll, B. (2023). The formation of chromite chains and clusters in igneous rocks. *Journal of Petrology* **64**(1). <https://doi.org/10.1093/petrology/egac124>.
- Huber, C. & Parmigiani, A. (2018). A physical model for three-phase compaction in silicic magma reservoirs. *Journal of Geophysical Research: Solid Earth* **123**, 2685–2705. <https://doi.org/10.1002/2017JB015224>.
- Humphreys, M. C. S. (2011). Silicate liquid immiscibility within the crystal mush: evidence from Ti in plagioclase from the Skaergaard intrusion. *Journal of Petrology* **52**(1), 147–174. <https://doi.org/10.1093/petrology/egq076>.
- Humphreys, M. C. S., Blundy, J. D. & Sparks, R. S. J. (2006). Magma evolution and open-system processes at Shiveluch Volcano: insights

- from phenocryst zoning. *Journal of Petrology* **47**(12), 2303–2334. <https://doi.org/10.1093/petrology/egl045>.
- Hunt, E. J., Finch, A. A. & Donaldson, C. H. (2017). Layering in peralkaline magmas, Ilímaussaq complex, S Greenland. *Lithos* **268–271**, 1–15. <https://doi.org/10.1016/j.lithos.2016.10.023>.
- Hunter, R. H. (1987) Textural equilibrium in layered igneous rocks. In: Parsons, I. (ed.) *Origins of Igneous Layering*, Vol. **196**. Dordrecht: Springer.
- Hunter, R. H. (1996). Texture development in cumulate rocks. *Developments in Petrology* **15**, 77–101. [https://doi.org/10.1016/S0167-2894\(96\)80005-4](https://doi.org/10.1016/S0167-2894(96)80005-4).
- Ikeda, S., Toriumi, M., Yoshida, H. & Shimizu, I. (2002). Experimental study of the textural development of igneous rocks in the late stage of crystallization: the importance of interfacial energies under non-equilibrium conditions. *Contributions to Mineralogy and Petrology* **142**(4), 397–415. <https://doi.org/10.1007/s004100100300>.
- Imon, R., Okudaira, T. & Fujimoto, A. (2002). Dissolution and precipitation processes in deformed amphibolites: an example from the ductile shear zone of the Ryoke metamorphic belt, SW Japan. *Journal of Metamorphic Petrology* **20**, 297–308. <https://doi.org/10.1046/j.1525-1314.2002.00367.x>.
- Irvine, T. N. (1980) Magmatic infiltration metasomatism, double-diffusive fractional crystallization, and adcumulus growth in the Muskox intrusion and other layered intrusions. In: Hargraves, R.B. (ed.) *Physics of Magmatic Processes*. New Jersey: Princeton University Press, pp. 325–383.
- Irvine, N. T., Andersen, J. C. O. & Brooks, K. C. (1998). Included blocks (and blocks within blocks) in the Skaergaard intrusion: geologic relations and the origins of rhythmic modally graded layers. *Geological Society of America Bulletin* **110**(11), 1398–1447. [https://doi.org/10.1130/0016-7606\(1998\)110<1398:IBABWB>2.3.CO;2](https://doi.org/10.1130/0016-7606(1998)110<1398:IBABWB>2.3.CO;2).
- Jackson, E. (1961). Primary textures and mineral associations in the ultramafic zone of the Stillwater complex. *Geological Survey Professional Paper* **358**, 1–103. <https://doi.org/10.3133/pp358>.
- Jackson, M. D., Blundy, J. & Sparks, R. S. J. (2018). Chemical differentiation, cold storage and remobilization of magma in the Earth's crust. *Nature* **564**(7736), 405–409. <https://doi.org/10.1038/s41586-018-0746-2>.
- Jerram, D. A., Cheadle, M. J. & Philpotts, A. R. (2003). Quantifying the building blocks of igneous rocks: are clustered crystal frameworks the foundation? *Journal of Petrology* **44**(11), 2033–2051. <https://doi.org/10.1093/petrology/egg069>.
- Ji, S. & Mainprice, D. (1990). Recrystallization and fabric development in plagioclase. *The Journal of Geology* **98**(1), 65–79. <https://doi.org/10.1086/629375>.
- Jones, E., McCarthy, W., Magee, C., Mattsson, T., Piazzolo, S., Hutchison, W. & Humphreys, M. C. S. (2025). Igneous layering and magma dynamics in alkaline intrusions: textural evidence for gravitational settling and compaction within cumulates. *Journal of the Geological Society* **182**. <https://doi.org/10.1144/jgs2024-181>.
- Kaur, P., Chaudhri, N., Hofmann, A. W., Raczek, I., Okrusch, M., Skora, S. & Baumgartner, L. P. (2012). Two-stage, extreme albitization of A-type granites from Rajasthan, NW India. *Journal of Petrology* **53**(5), 919–948. <https://doi.org/10.1093/petrology/egs003>.
- Kerr, R. C. & Tait, S. R. (1986). Crystallization and compositional convection in a porous medium with application to layered igneous intrusions. *Journal of Geophysical Research: Solid Earth* **91**(B3), 3591–3608. <https://doi.org/10.1029/jb091ib03p03591>.
- Koehn, D., Piazzolo, S., Beaudoin, N., Kelka, U., Spruženiece, L., Putnis, C. & Toussaint, R. (2021). Relative rates of fluid advection, elemental diffusion and replacement govern reaction front patterns. *Earth and Planetary Science Letters* **565**, 116950. <https://doi.org/10.1016/j.epsl.2021.116950>.
- Konnerup-Madsen, J. & Rose-Hansen, J. (1982). Volatiles associated with alkaline igneous rift activity: fluid inclusions in the Ilímaussaq intrusion and the Gardar granitic complexes (South Greenland). *Chemical Geology* **37**, 79–93. [https://doi.org/10.1016/0009-2541\(82\)90068-7](https://doi.org/10.1016/0009-2541(82)90068-7).
- Konnerup-Madsen, J., Larsen, E. & Rose-Hansen, J. (1979). Hydrocarbon-rich fluid inclusions in minerals from the alkaline Ilímaussaq intrusion, South Greenland. *Bulletin de Minéralogie* **102**(5), 642–653. <https://doi.org/10.3406/bulmi.1979.7313>.
- Koopmans, L., McCarthy, W. & Magee, C. (2022). Dyke architecture, mineral layering, and magmatic convection; new perspectives from the Younger Giant Dyke complex, S Greenland. *Geochemistry, Geophysics, Geosystems* **23**(3). <https://doi.org/10.1029/2021GC010260>.
- Krumrei, T. V., Villa, I. M., Marks, M. A. W. & Markl, G. (2006). A ⁴⁰Ar/³⁹Ar and U/Pb isotopic study of the Ilímaussaq complex, South Greenland: implications for the 40K decay constant and for the duration of magmatic activity in a peralkaline complex. *Chemical Geology* **227**(3–4), 258–273. <https://doi.org/10.1016/j.chemgeo.2005.10.004>.
- Larsen, L. M. (1976). Clinopyroxenes and coexisting mafic minerals from the alkaline Ilímaussaq intrusion, South Greenland. *Journal of Petrology* **17**, 258–290. <https://doi.org/10.1093/petrology/17.2.258>.
- Larsen, L. M. (1977). Aenigmatites from the Ilímaussaq intrusion, South Greenland: chemistry and petrological implications. *Lithos* **10**, 257–270. [https://doi.org/10.1016/0024-4937\(77\)90002-0](https://doi.org/10.1016/0024-4937(77)90002-0).
- Larsen, L. M. & Sørensen, H. (1987). The Ilímaussaq intrusion - progressive crystallization and formation of layering in an agpaite magma. *Geological Society Special Publication* **30**, 473–488. <https://doi.org/10.1144/GSL.SP.1987.030.01.23>.
- Latypov, R. M., Chistyakova, S. Y., Namur, O., & Barnes, S. (2020). Dynamics of evolving magma chambers: textural and chemical evolution of cumulates at the arrival of new liquidus phases. *Earth-Science Reviews* **210**, 103388. <https://doi.org/10.1016/j.earscirev.2020.103388>.
- Latypov, R. M., Namur, O., Bai, Y., Barnes, S. J., Chistyakova, S., Holness, M. B., Iacono-Marziano, G., Kruger, W. A. J., O'Driscoll, B., Smith, W. D., Virtanen, V. J., Wang, C. Y., Xing, C. M. & Charlier, B. (2024). Layered intrusions: fundamentals, novel observations and concepts, and controversial issues. *Earth-Science Reviews* **249**, 104653. <https://doi.org/10.1016/j.earscirev.2023.104653>.
- Law, R. D. (1990). Crystallographic fabrics: a selective review of their applications to research in structural geology. *Geological Society Special Publication* **54**, 335–352. <https://doi.org/10.1144/GSL.SP.1990.054.01.30>.
- Lee, M. R. & Parsons, I. (1997). Dislocation formation and albitization in alkali feldspars from the Shap granite. *American Mineralogist* **82**, 557–570. <https://doi.org/10.2138/am-1997-5-616>.
- Lee, A. L., Stünitz, H., Soret, M. & Battisti, M. A. (2022). Dissolution precipitation creep as a process for the strain localisation in mafic rocks. *Journal of Structural Geology* **155**, 104505. <https://doi.org/10.1016/j.jsg.2021.104505>.
- Leuthold, J., Blundy, J. D., Holness, M. B. & Sides, R. (2014). Successive episodes of reactive liquid flow through a layered intrusion (unit 9, Rum eastern layered intrusion, Scotland). *Contributions to Mineralogy and Petrology* **168**(1), 1–27. <https://doi.org/10.1007/s00410-014-1021-7>.
- Lindhuber, M. J., Marks, M. A. W., Bons, P. D., Wenzel, T. & Markl, G. (2015). Crystal mat-formation as an igneous layering-forming process: textural and geochemical evidence from the “lower layered” nepheline syenite sequence of the Ilímaussaq complex,

- South Greenland. *Lithos* **224–225**, 295–309. <https://doi.org/10.1016/j.lithos.2015.03.007>.
- Lissenberg, C. J. & MacLeod, C. J. (2016). A reactive porous flow control on mid-ocean ridge magmatic evolution. *Journal of Petrology* **57**(11–12), 2195–2220. <https://doi.org/10.1093/petrology/egw074>.
- Lissenberg, C. J., MacLeod, C. J. & Bennett, E. N. (2019). Consequences of a crystal mush-dominated magma plumbing system: a mid-ocean ridge perspective. *Philosophical Transactions of the Royal Society A: Mathematical, Physical and Engineering Sciences* **377**(2139), 20180014. <https://doi.org/10.1098/rsta.2018.0014>.
- Lister, G. S. & Hobbs, B. E. (1980). The simulation of fabric development during plastic deformation and its application to quartzite: the influence of deformation history. *Journal of Structural Geology* **2**, 355–370. [https://doi.org/10.1016/0191-8141\(80\)90023-1](https://doi.org/10.1016/0191-8141(80)90023-1).
- Mangler, M. F., Humphreys, M. C. S., Iveson, A. A., Cooper, K. M., Clyne, M. A., Lindoo, A., Brooker, R. A. & Wadsworth, F. B. (2024). Crystal resorption as a driver for mush maturation: an experimental investigation. *Journal of Petrology* **65**(9). <https://doi.org/10.1093/petrology/egae088>.
- Markl, G., Marks, M., Schwinn, G. & Sommer, H. (2001). Phase equilibrium constraints on intensive crystallization parameters of the Ílímaussaq complex, South Greenland. *Journal of Petrology* **42**, 2231–2257. <https://doi.org/10.1093/petrology/42.12.2231>.
- Marks, M. A. W. & Markl, G. (2015) The Ílímaussaq alkaline complex, South Greenland. In: Charlier et al. (eds) *Layered Intrusions*. Dordrecht: Springer, pp. 649–691.
- Marks, M. A. W. & Markl, G. (2017). A global review on agpaitic rocks. *Earth-Science Reviews* **173**, 229–258. <https://doi.org/10.1016/j.earscirev.2017.06.002>.
- Marsh, J. S., Pasieczny, M. J. & Boudreau, A. E. (2021). Formation of chromitite seams and associated anorthosites in layered intrusion by reactive volatile-rich fluid infiltration. *Journal of Petrology* **62**(2). <https://doi.org/10.1093/petrology/egaa109>.
- Mathez, E. A., Hunter, R. H. & Kinzler, R. (1997). Petrologic evolution of partially molten cumulate: the Atok section of the Bushveld complex. *Contributions to Mineralogy and Petrology* **129**(129), 20–34. <https://doi.org/10.1007/s004100050320>.
- McCarthy, A., Chelle-Michou, C., Blundy, J. D., Vonlanthen, P., Meibom, A. & Escrig, S. (2020). Taking the pulse of volcanic eruptions using plagioclase glomerocrysts. *Earth and Planetary Science Letters* **552**, 116596. <https://doi.org/10.1016/j.epsl.2020.116596>.
- Mckenzie, D. (1984). The generation and compaction of partially molten rock. *Journal of Petrology* **25**, 713–765. <https://doi.org/10.1093/petrology/25.3.713>.
- Mckenzie, D. (2011). Compaction and crystallization in magma chambers: towards a model of the Skaergaard intrusion. *Journal of Petrology* **52**(5), 905–930. <https://doi.org/10.1093/petrology/egr009>.
- Mei, S., Bai, W., Hiraga, T. & Kohlstedt, D. L. (2002). Influence of melt on the creep behavior of olivine basalt aggregates under hydrous conditions. *Earth and Planetary Science Letters* **201**, 491–507. [https://doi.org/10.1016/S0012-821X\(02\)00745-8](https://doi.org/10.1016/S0012-821X(02)00745-8).
- Meurer, W. P. & Boudreau, A. E. (1996). Compaction of density-stratified cumulates: effect on trapped-liquid distribution. *The Journal of Geology* **104**(1), 115–120. <https://doi.org/10.1086/629805>.
- Meurer, W. P. & Boudreau, A. E. (1998a). Compaction of igneous cumulates part I: geochemical consequences for cumulates and liquid fractionation trends. *Journal of Geology* **106**(3), 281–292. <https://doi.org/10.1086/516022>.
- Meurer, W. P. & Boudreau, A. E. (1998b). Compaction of igneous cumulates part II: compaction and the development of igneous foliations. *The Journal of Geology* **106**(3), 293–304. <https://doi.org/10.1086/516023>.
- Meurer, W. P., Willmore, C. C. & Boudreau, A. E. (1999). Metal redistribution during fluid exsolution and migration in the middle banded series of the Stillwater complex, Montana. *Lithos* **47**, 143–156. [https://doi.org/10.1016/S0024-4937\(99\)00012-2](https://doi.org/10.1016/S0024-4937(99)00012-2).
- Moore, A., Coogan, L. A., Costa, F. & Perfit, M. R. (2014). Primitive melt replenishment and crystal-mush disaggregation in the weeks preceding the 2005–2006 eruption 9°50' N, EPR. *Earth and Planetary Science Letters* **403**, 15–26. <https://doi.org/10.1016/j.epsl.2014.06.015>.
- Nakamura, M. & Shimakita, S. (1998). Dissolution origin and syn-entrapment compositional change of melt inclusion in plagioclase. *Earth and Planetary Science Letters* **161**, 119–133. [https://doi.org/10.1016/S0012-821X\(98\)00144-7](https://doi.org/10.1016/S0012-821X(98)00144-7).
- Nicolas, A. (1992). Kinematics in magmatic rocks with special reference to gabbros. *Journal of Petrology* **33**, 891–915. <https://doi.org/10.1093/petrology/33.4.891>.
- Nikolenko, A., Schmidt, C., Sieber, M. J., van Schijndel, V. & Veksler, I. V. (2024). Magmatic stability of eudialyte-group minerals (EGM) and element distribution between EGM and peralkaline silica-undersaturated melts. *Lithos* **490–491**, 107839. <https://doi.org/10.1016/j.lithos.2024.107839>.
- O'Driscoll, B., Hargraves, R. B., Emeleus, C. H., Troll, V. R., Donaldson, C. H. & Reavy, R. J. (2007). Magmatic lineations inferred from anisotropy of magnetic susceptibility fabrics in units 8, 9, and 10 of the Rum eastern layered series, NW Scotland. *Lithos* **98**(1–4), 27–44. <https://doi.org/10.1016/j.lithos.2007.01.009>.
- O'Driscoll, B., Stevenson, C. T. E. & Troll, V. R. (2008). Mineral lamination development in layered gabbros of the British palaeogene igneous province: a combined anisotropy of magnetic susceptibility, quantitative textural and mineral chemistry study. *Journal of Petrology* **49**(6), 1187–1221. <https://doi.org/10.1093/petrology/egn022>.
- O'Driscoll, B., Petronis, M. S., Marks, M. A. W., McCarthy, W. S., Mariani, E., Stevenson, C. T. E., Clay, P. L. & Geissman, J. W. (2024). Magnetic fabrics in laminated rocks of the Ílímaussaq igneous complex, southern Greenland. *The Canadian Journal of Mineralogy and Petrology* **62**, 821–846. <https://doi.org/10.3749/2400008>.
- Oppenheimer, J., Rust, A. C., Cashman, K. V. & Sandnes, B. (2015). Gas migration regimes and outgassing in particle-rich suspensions. *Frontiers in Physics* **3**(AUG). <https://doi.org/10.3389/fphy.2015.00060>.
- Parmigiani, A., Huber, C., Bachmann, O. & Chopard, B. (2011). Pore-scale mass and reactant transport in multiphase porous media flows. *Journal of Fluid Mechanics* **686**, 40–76. <https://doi.org/10.1017/jfm.2011.268>.
- Parmigiani, A., Faroughi, S., Huber, C., Bachmann, O. & Su, Y. (2016). Bubble accumulation and its role in the evolution of magma reservoirs in the upper crust. *Nature* **532**(7600), 492–495. <https://doi.org/10.1038/nature17401>.
- Parsons, I. (1979). The Klokken gabbro-syenite complex, South Greenland: cryptic variation and origin of inversely graded layering. *Journal of Petrology* **20**, 653–694. <https://doi.org/10.1093/petrology/20.4.653>.
- Passchier, C. W. & Trouw, R. A. J. (2005) *Microtectonics*, 2nd edn. Heidelberg: Springer.
- Paterson, M. S. (1973). Nonhydrostatic thermodynamics and its geologic applications. *Reviews of Geophysics and Space Physics* **11**(2), 355–389. <https://doi.org/10.1029/RG011i002p00355>.
- Paterson, M. S. (2001). A granular flow theory for the deformation of partially molten rock. *Tectonophysics* **335**, 51–61. [https://doi.org/10.1016/S0040-1951\(01\)00045-2](https://doi.org/10.1016/S0040-1951(01)00045-2).

- Petersen, O. V. (2001). List of all minerals identified in the Ilímaussaq alkaline complex, South Greenland. *Geology of Greenland Survey Bulletin*, **190**, 25–33. <https://doi.org/10.34194/ggub.v190.5171>.
- Petford, N., Cruden, A. R., Mccaffrey, K. J. W. & Vigneresse, J. L. (2000). Granite magma formation, transport and emplacement in the Earth's crust. *Nature* **408**, 669–673. <https://doi.org/10.1038/35047000>.
- Pfaff, K., Krumrei, T., Marks, M., Wenzel, T., Rudolf, T. & Markl, G. (2008). Chemical and physical evolution of the “lower layered sequence” from the nepheline syenitic Ilímaussaq intrusion, South Greenland: implications for the origin of magmatic layering in peralkaline felsic liquids. *Lithos* **106**(3–4), 280–296. <https://doi.org/10.1016/j.lithos.2008.07.018>.
- Philpotts, A. R. & Philpotts, D. E. (2005). Crystal-mush compaction in the Cohasset flood-basalt flow, Hanford, Washington. *Journal of Volcanology and Geothermal Research* **145**(3–4), 192–206. <https://doi.org/10.1016/j.jvolgeores.2005.01.008>.
- Philpotts, A. R., Shi, J. & Brustman, C. (1998). Role of plagioclase crystal chains in the differentiation of partly crystallized basaltic magma. *Nature* **395**, 343–346. <https://doi.org/10.1038/26404>.
- Piazolo, S., Jessell, M. W., Prior, D. J. & Bons, P. D. (2004). The integration of experimental in-situ EBSD observations and numerical simulations: a novel technique of microstructural process analysis. *Journal of Microscopy* **213**(3), 273–284. <https://doi.org/10.1111/j.0022-2720.2004.01304.x>.
- Piazolo, S., Prior, D. J. & Holness, M. D. (2005). The use of combined cathodoluminescence and EBSD analysis: a case study investigating grain boundary migration mechanisms in quartz. *Journal of Microscopy* **217**(2), 152–161. <https://doi.org/10.1111/j.1365-2818.2005.01423.x>.
- Piazolo, S., Kaminsky, F. V., Trimby, P., Evans, L. & Luzin, V. (2016). Carbonado revisited: insights from neutron diffraction, high resolution orientation mapping and numerical simulations. *Lithos* **265**, 244–256. <https://doi.org/10.1016/j.lithos.2016.09.011>.
- Piotrowski, J. M. & Edgar, A. D. (1970). Melting relations of undersaturated alkaline rocks from South Greenland. *Meddelelser om Grønland* **181**(9), 1–62.
- Putnis, A. (2002). Mineral replacement reactions: from macroscopic observations to microscopic mechanisms. *Mineralogical Magazine* **66**(5), 689–708. <https://doi.org/10.1180/0026461026650056>.
- Putnis, A. (2009). Mineral replacement reactions. *Reviews in Mineralogy and Geochemistry* **70**, 87–124. <https://doi.org/10.2138/rmg.2009.70.3>.
- Ratschbacher, B. C., Marks, M. A. W., Bons, P. D., Wenzel, T. & Markl, G. (2015). Emplacement and geochemical evolution of highly evolved syenites investigated by a combined structural and geochemical field study: the lujavrites of the Ilímaussaq complex, SW Greenland. *Lithos* **231**, 62–76. <https://doi.org/10.1016/j.lithos.2015.06.004>.
- Rosenberg, C. L. (2001). Deformation of partially molten granite: a review and comparison of experimental and natural case studies. *International Journal of Earth Sciences* **90**(1), 60–76. <https://doi.org/10.1007/s005310000164>.
- Rutter, E. H. (1983). Pressure solution in nature, theory and experiment. *Journal of the Geological Society* **140**(5), 725–740. <https://doi.org/10.1144/gsjgs.140.5.0725>.
- Rybacki, E. & Dresen, G. (2004). Deformation mechanism maps for feldspar rocks. *Tectonophysics* **382**(3–4), 173–187. <https://doi.org/10.1016/j.tecto.2004.01.006>.
- Sanfilippo, A., MacLeod, C. J., Tribuzio, R., Lissenberg, C. J. & Zanetti, A. (2020). Early-stage melt-rock reaction in a cooling crystal mush beneath a slow-spreading mid-ocean ridge (IODP hole U1473A, Atlantis Bank, southwest Indian ridge). *Frontiers in Earth Science* **8**. <https://doi.org/10.3389/feart.2020.579138>.
- Satsukawa, Ildefonse, B., Mainprice, D., Morales, L. F. G., Michibayashi, K. & Barou, F. (2013). A database of plagioclase crystal preferred orientations (CPO) and microstructures-implications for CPO origin, strength, symmetry and seismic anisotropy in gabbroic rocks. *Solid Earth* **4**(2), 511–542. <https://doi.org/10.5194/se-4-511-2013>.
- Schmidt, M. W., Forien, M., Solferino, G. & Bagdassarov, N. (2012). Settling and compaction of olivine in basaltic magmas: an experimental study on the time scales of cumulate formation. *Contributions to Mineralogy and Petrology* **164**(6), 959–976. <https://doi.org/10.1007/s00410-012-0782-0>.
- Schönwandt, H. K., Barnes, G. B. & Ulrich, T. (2016) A description of the world-class rare earth element deposit, Tanbreez, South Greenland. In: Borges de Lima, I & Filho, W.L. (eds) *Rare Earths Industry: Technological, Economic, and Environmental Implications*. Boston: Elsevier, pp. 73–85.
- Schönwandt, H. K., Barnes, G. B. & Ulrich, T. (2023). Perthite in nepheline syenite from the kakortokite unit in the Ilímaussaq complex, South Greenland. *Journal of Geosciences* **68**(3), 203–211. <https://doi.org/10.3190/jgeosci.375>.
- Schwindinger, K. R. (1999). Particle dynamics and aggregation of crystals in a magma chamber with application to Kilauea Iki olivines. *Journal of Volcanology and Geothermal Research* **88**, 209–238. [https://doi.org/10.1016/S0377-0273\(99\)00009-8](https://doi.org/10.1016/S0377-0273(99)00009-8).
- Scott, T. & Kohlstedt, D. L. (2006). The effect of large melt fraction on the deformation behavior of peridotite. *Earth and Planetary Science Letters* **246**(3–4), 177–187. <https://doi.org/10.1016/j.epsl.2006.04.027>.
- Seaman, S. J. (2000). Crystal clusters, feldspar glomerocrysts, and magma envelopes in the Atascosa Lookout lava flow, southern Arizona, USA: recorders of magmatic events. *Journal of Petrology* **41**, 693–716. <https://doi.org/10.1093/petrology/41.5.693>.
- Shea, T. & Hammer, J. E. (2013). Kinetics of cooling- and decompression-induced crystallization in hydrous mafic-intermediate magmas. *Journal of Volcanology and Geothermal Research* **260**, 127–145. <https://doi.org/10.1016/j.jvolgeores.2013.04.018>.
- Shirley, D. N. (1986). Compaction of igneous cumulates. *Journal of Geology* **94**, 795–809. <https://doi.org/10.1086/629088>.
- Sisson, T. W. & Bacon, C. R. (1999). Gas-driven filter pressing in magmas. *Geology* **27**, 613–616. [https://doi.org/10.1130/0091-7613\(1999\)027<0613:GDFPIM>2.3.CO;2](https://doi.org/10.1130/0091-7613(1999)027<0613:GDFPIM>2.3.CO;2).
- Sliwinski, J. T., Bachmann, O., Ellis, B. S., Dávila-Harris, P., Nelson, B. K. & Dufek, J. (2015). Eruption of shallow crystal cumulates during explosive phonolitic eruptions on Tenerife, Canary Islands. *Journal of Petrology* **56**(11), 2173–2194. <https://doi.org/10.1093/petrology/egv068>.
- Smith, W. D. & Maier, W. D. (2021). The geotectonic setting, age and mineral deposit inventory of global layered intrusions. *Earth-Science Reviews* **220**, 1–36. <https://doi.org/10.1016/j.earscirev.2021.103736>.
- Solano, J. M. S., Jackson, M. D., Sparks, R. S. J. & Blundy, J. (2014). Evolution of major and trace element composition during melt migration through crystalline mush: implications for chemical differentiation in the crust. *American Journal of Science* **314**(5), 895–939. <https://doi.org/10.2475/05.2014.01>.
- Sood, M. K. & Edgar, A. D. (1970). Melting relations of undersaturated alkaline rocks. *Meddelelser om Grønland* **181**(12), 1–41.
- Sorensen, H. (1992). Agpaitic nepheline syenites: a potential source of rare elements. *Applied Geochemistry* **7**, 417–427. [https://doi.org/10.1016/0883-2927\(92\)90003-L](https://doi.org/10.1016/0883-2927(92)90003-L).

- Sorensen, H. (1997). The agpaite rocks - an overview. *Mineralogical Magazine* **61**, 485–498. <https://doi.org/10.1180/minmag.1997.061.407.02>.
- Sørensen, H. (2001). Brief introduction to the geology of the Ilímaussaq alkaline complex, South Greenland, and its exploration history. *Geology of Greenland Survey Bulletin* **190**, 7–23. <https://doi.org/10.34194/ggub.v190.5170>.
- Sørensen, H., Bailey, J. C., Kogarko, L. N., Rose-Hansen, J. & Karup-Møller, S. (2003). Spheroidal structures in arfvedsonite lujavrite, Ilímaussaq alkaline complex, South Greenland—an example of macro-scale liquid immiscibility. *Lithos* **70**(1–2), 1–20. [https://doi.org/10.1016/S0024-4937\(03\)00086-0](https://doi.org/10.1016/S0024-4937(03)00086-0).
- Sørensen, H., Bohse, H. & Bailey, J. C. (2006). The origin and mode of emplacement of lujavrites in the Ilímaussaq alkaline complex, South Greenland. *Lithos* **91**(1–4), 286–300. <https://doi.org/10.1016/j.lithos.2006.03.021>.
- Sparks, R. S. J., Huppert, H. E., Kerr, R. C., McKenzie, D. P. & Tait, S. R. (1985). Postcumulus processes in layered intrusions. *Geological Magazine* **122**(5), 555–568. <https://doi.org/10.1017/S0016756800035470>.
- Spiegelman, M., Kelemen, P. B. & Aharonov, E. (2001). Causes and consequences of flow organization during melt transport: the reaction infiltration instability in compactible media. *Journal of Geophysical Research: Solid Earth* **106**(B2), 2061–2077. <https://doi.org/10.1029/2000jb900240>.
- Špillar, V. & Dolejš, D. (2015). Heterogeneous nucleation as the predominant mode of crystallization in natural magmas: numerical model and implications for crystal–melt interaction. *Contributions to Mineralogy and Petrology* **169**(1). <https://doi.org/10.1007/s00410-014-1103-6>.
- Spruzenie, L., Piazzolo, S. & Maynard-Casely, H. E. (2017). Deformation-resembling microstructure created by fluid-mediated dissolution-precipitation reactions. *Nature Communications* **8**. <https://doi.org/10.1038/ncomms14032>.
- Stewart, M. L. & Pearce, T. H. (2004). Sieve-textured plagioclase in dacitic magma: interference imaging results. *American Mineralogist* **89**, 348–351. <https://doi.org/10.2138/am-2004-2-313>.
- Streck, M. J. (2008). Mineral textures and zoning as evidence for open system processes. *Reviews in Mineralogy and Geochemistry* **69**, 595–622. <https://doi.org/10.2138/rmg.2008.69.15>.
- Stünitz, H., Fitz Gerald, J. D. & Tullis, J. (2003). Dislocation generation, slip systems, and dynamic recrystallization in experimentally deformed plagioclase single crystals. *Tectonophysics* **372**(3–4), 215–233. [https://doi.org/10.1016/S0040-1951\(03\)00241-5](https://doi.org/10.1016/S0040-1951(03)00241-5).
- Stünitz, H., Neufeld, K., Heilbronner, R., Finstad, A. K., Konopásek, J. & Mackenzie, J. R. (2020). Transformation weakening: diffusion creep in eclogites as a result of interaction of mineral reactions and deformation. *Journal of Structural Geology* **139**, 104129. <https://doi.org/10.1016/j.jsg.2020.104129>.
- Svahnberg, H. & Piazzolo, S. (2010). The initiation of strain localisation in plagioclase-rich rocks: insights from detailed microstructural analyses. *Journal of Structural Geology* **32**(10), 1404–1416. <https://doi.org/10.1016/j.jsg.2010.06.011>.
- Svahnberg, H. & Piazzolo, S. (2013). Interaction of chemical and physical processes during deformation at fluid-present conditions: a case study from an orthosite-leucogabbro deformed at amphibolite facies conditions. *Contributions to Mineralogy and Petrology* **165**(3), 543–562. <https://doi.org/10.1007/s00410-012-0822-9>.
- Tait, S. & Jaupart, C. (1992). Compositional convection in a reactive crystalline mush and melt differentiation. *Journal of Geophysical Research* **97**(B5), 6735–6756. <https://doi.org/10.1029/92JB00016>.
- Tavazzani, L., Peres, S., Sinigoi, S., Demarchi, G., Economos, R. C. & Quick, J. E. (2020). Timescales and mechanisms of crystal-mush rejuvenation and melt extraction recorded in Permian plutonic and volcanic rocks of the Sesia magmatic system (southern Alps, Italy). *Journal of Petrology* **61**(5). <https://doi.org/10.1093/petrology/egaa049>.
- Tegner, C., Thy, P., Holness, M. B., Jakobsen, J. K. & Leshner, C. E. (2009). Differentiation and compaction in the Skaergaard intrusion. *Journal of Petrology* **50**(5), 813–840. <https://doi.org/10.1093/petrology/egp020>.
- Tepper, J. H. & Kuehner, S. M. (1999). Complex zoning in apatite from the Idaho batholith: a record of magma mixing and intracrystalline trace element diffusion. *American Mineralogist* **84**(4), 581–595. <https://doi.org/10.2138/am-1999-0412>.
- Tharp, T. M., Loucks, R. R. & Sack, R. O. (1998). Modeling compaction of olivine cumulates in the Muskox intrusion. *American Journal of Science* **298**, 758–790. <https://doi.org/10.2475/ajs.298.9.758>.
- Thy, P., Leshner, C. E. & Tegner, C. (2009). The Skaergaard liquid line of descent revisited. *Contributions to Mineralogy and Petrology* **157**(6), 735–747. <https://doi.org/10.1007/s00410-008-0361-6>.
- Torquato, S., Truskett, T. M. & Debenedetti, P. G. (2000). Is random close packing of spheres well defined? *Physical Review Letters* **84**, 2064–2067. <https://doi.org/10.1103/PhysRevLett.84.2064>.
- Tullis, J. & Yund, R. A. (1991). Diffusion creep in feldspar aggregates: experimental evidence. *Journal of Structural Geology* **13**(9), 987–1000. [https://doi.org/10.1016/0191-8141\(91\)90051-J](https://doi.org/10.1016/0191-8141(91)90051-J).
- Upton, B. G. J. (2013). Tectono-magmatic evolution of the younger Gardar southern rift, South Greenland. *Geological Survey of Denmark and Greenland Bulletin* **29**, 1–124. <https://doi.org/10.34194/geusb.v29.4692>.
- Upton, B. G. J., Emeleus, C. H., Heaman, L. M., Goodenough, K. M. & Finch, A. A. (2003). Magmatism of the mid-Proterozoic Gardar Province, South Greenland: chronology, petrogenesis and geological setting. *Lithos* **68**(1–2), 43–65. [https://doi.org/10.1016/S0024-4937\(03\)00030-6](https://doi.org/10.1016/S0024-4937(03)00030-6).
- Urai, J. L., Means, W. D. & Lister, G. S. (1986) Dynamic Recrystallization of Minerals. *Mineral and Rock Deformation*, **36**, 161–199. <https://doi.org/10.1029/GM036p0161>.
- Vernon, R. H. (1968). Microstructures of high-grade metamorphic rocks at Broken Hill, Australia. *Journal of Petrology* **9**(1), 1–22. <https://doi.org/10.1093/petrology/9.1.1>.
- Vernon, R. H. (2004) *A Practical Guide Book to Rock Microstructure*. Cambridge: Cambridge University Press.
- Vernon, R. H. & Paterson, S. R. (2008). How extensive are subsolidus grain-shape changes in cooling granites? *Lithos* **105**(1–2), 42–50. <https://doi.org/10.1016/j.lithos.2008.02.004>.
- Vukmanovic, Z., Holness, M. B., Stock, M. J. & Roberts, R. J. (2019). The creation and evolution of crystal mush in the upper zone of the Rustenburg layered suite, Bushveld complex, South Africa. *Journal of Petrology* **60**(8), 1523–1542. <https://doi.org/10.1093/petrology/egz038>.
- Wager, L. R. (1963) The Mechanism of Adcumulus Growth in the Layered Series of the Skaergaard Intrusion. In: *Mineralogical Society of America Special Paper* **1**, 1–9.
- Wager, L. R., Brown, G. M. & Wadsworth, W. J. (1960). Types of igneous cumulates. *Journal of Petrology* **1**(1), 73–85. <https://doi.org/10.1093/petrology/1.1.73>.
- Weller, O. M., Holland, T. J. B., Soderman, C. R., Green, E. C. R., Powell, R., Beard, C. D. & Riel, N. (2024). New thermodynamic models for anhydrous alkaline-silicate magmatic systems. *Journal of Petrology* **65**(10). <https://doi.org/10.1093/petrology/egae098>.
- Zeng, Q. & Xu, S. (2015). Thermodynamics and characteristics of heterogeneous nucleation on fractal surfaces. *Journal of Physical Chemistry C* **119**(49), 27426–27433. <https://doi.org/10.1021/acs.jpcc.5b07709>.

Zhang, W. Q. & Liu, C. Z. (2023). Crust-scale reactive porous flow revealed by the brown amphibole in the IODP hole U1473A gabbros, southwest Indian ridge. *Lithos* **450-451**, 107209. <https://doi.org/10.1016/j.lithos.2023.107209>.

Zhu, Y. X., Wang, L. X., Ma, C. Q. & Zhang, C. (2018). A flower-like glomerophytic diorite porphyry from Central China: constraints on the unusual texture. *Lithos* **318-319**, 1–13. <https://doi.org/10.1016/j.lithos.2018.07.031>.